[American Journal of Science, Vol. 303, June, 2003, P. 489–518]

American Journal of Science

JUNE 2003

POST-OROGENIC EVOLUTION OF THE DABIE SHAN, EASTERN CHINA, FROM (U-Th)/He AND FISSION-TRACK THERMOCHRONOLOGY

PETER W. REINERS*, ZUYI ZHOU**, TODD A. EHLERS***, CHANGHAI XU**, MARK T. BRANDON*, RAYMOND A. DONELICK****, AND STEFAN NICOLESCU*

ABSTRACT. The Dabie Shan of eastern China is a ~200 kilometers wide mountain range with nearly 2 kilometers of relief and is an archetype of deep ultrahigh-pressure metamorphic rock exhumation. Despite its regional and petrologic importance, little is known about the low-temperature and post-orogenic evolution of the Dabie Shan. Here we present apatite and zircon (U-Th)/He (AHe and ZHe, respectively) and apatite fission-track (AFT) cooling ages from the Dabie Shan that constrain the patterns and history of exhumation over the last ~115 myr. On the scale of the whole orogen, ZHe and AHe ages are inversely correlated with mean elevation and are systematically younger in the core of the range. These cooling ages were converted to exhumation rates assuming steady-state erosion and accounting for topographic effects. These results indicate that, since the Eocene, flanks of the range have eroded at rates as low as 0.02 km/myr, while the range core has eroded at about 0.06 km/myr. Even in the core of the range, these recent exhumation rates are at least 10 to 20 times slower than those estimated for the initial stages of exhumation in the Triassic-Jurassic. In a 1.4 kilometer vertical transect in the core of the range, all ages are positively correlated with elevation, with ZHe ages increasing from 76 to 112 Ma, AFT from 44 to 70 Ma, and AHe from 24 to 43 Ma. We present a simple model for topographic correction of thermochronometric ages in vertical transects, using the admittance ratio (ratio of isotherm relief to topographic relief). Applied to the AHe age-elevation relationship, this yields Tertiary exhumation rates of 0.05 to 0.07 km/myr in the core of the Dabie Shan, in good agreement with regional exhumation rate patterns. Finally, age-elevation relationships for all three chronometers in the vertical transect are consistent with a constant exhumation rate of 0.06 ± 0.01 km/myr since the Cretaceous, with a possible modest increase in exhumation rates (as high as 0.2 km/myr) between 80 to 40 Ma. These data show no evidence for significant variations in exhumation rates over the last ~115 myr, as might be expected for decay of old topography or tectonic reactivation of old structures.

INTRODUCTION

Collisional orogenies typically produce topographic and geophysical anomalies persisting several hundred million years. The post-orogenic evolution of mountain ranges and their responses to erosion and subsequent tectonic events provides insights to a variety of problems, including the deep crustal architecture of orogens, dynamics of lithospheric roots, and the erosional decay of topographic anomalies. Typically, the topographic and structural decay of an ancient mountain range is not monotonic, and

*Department of Geology and Geophysics, Yale University, P.O. Box 208109, New Haven, Connecticut 06520-8109, USA; peter.reiners@yale.edu
**MOE Lab of Marine Geology, Tongji University, Shanghai 200092, China
***Department of Geological Sciences, University of Michigan, Ann Arbor, Michigan 48109, USA
****Apatite to Zircon, Inc., Viola, Idaho 83872, USA

characteristics such as topographic relief, lithospheric structure, and erosional fluxes change in response to post-orogenic deformation, climatic changes, fluvial adjustments, or convective instabilities (for example, Pazzaglia and Brandon, 1996; Ducea and Saleeby, 1998; Ratschbacher and others, 2000; Jull and Kelemen, 2001; Baldwin and others, 2003). In some cases, post-orogenic dynamics of ancient ranges may record effects of relatively subtle or far-field tectonic activity or climatic changes, because these high-relief regions are susceptible to subtle erosion rate changes, which can be quantified with low-temperature thermochronometry such as (U-Th)/He or fission-track dating.

This study examines the post-orogenic evolution of the Dabie Shan of eastern China, an early Mesozoic mountain range whose initial high-temperature evolution is well-studied following the discovery of diamond- and coesite-bearing crustal rocks there. Here we present results and interpretations of the low-temperature post-orogenic history of the Dabie Shan, using apatite and zircon (U-Th)/He (AHe and ZHe, respectively) and apatite fission-track (AFT) thermochronometry. The goal is to constrain the timing and rates of shallow crustal exhumation since the last major orogenic episode (mid-Cretaceous). Other than a previous study with four zircon (U-Th)/He ages (Kirby and others, 2002), this study represents the first regional application of zircon (U-Th)He thermochronometry to understand orogenic exhumation, and our results support previous interpretations suggesting that ZHe ages can be assumed to represent cooling ages associated with an effective closure temperature of $180° \pm 20°C$.

In interpreting these data we demonstrate the use of three different and relatively simple methods for interpreting topography-corrected exhumation rates from low-temperature thermochronologic ages. The first method interprets exhumation rates from isolated ages in the context of a steady exhumation rate model that accounts for closure depth variations arising from variable cooling rates, topography above a critical wavelength, and other effects (Brandon and others, 1998). This method is used to demonstrate a strong cross-range gradient in exhumation rates in the Dabie Shan. The second method interprets exhumation rates from age-elevation relationships of vertical transects by correcting for topographic effects (for example, Stüwe and others, 1994; Mancktelow and Grasemann, 1997) using the admittance ratio (the ratio of isotherm to topographic relief). Admittance ratio has been introduced by Braun (2002a) for assessing temporal changes in topographic relief; here we use it to correct for topographic effects on age-elevation relationships as a function of topographic wavelength and closure temperature. Our method makes use of the fact that admittance is largely independent of topographic relief, thus providing a useful and easily-applied correction for vertical-transect data. Finally, we directly model the thermal evolution of samples in the vertical transect using production-diffusion and annealing models, allowing for different thermal histories caused by topography in the latest stages of exhumation. Application of all three of these methods indicate that exhumation since at least the mid-Tertiary in the core of the Dabie Shan has been 0.06 ± 0.01 km/myr.

TECTONIC SETTING

The Dabie Shan of east-central China (fig. 1) lies at the eastern terminus of the currently contiguous part of a ~2000 kilometer long orogenic belt of generally subdued topographic relief (<2 km), extending from the Dabie Shan west towards the northern edge of the Tibetan plateau. Over most of its length, this belt is interpreted as the Triassic suture zone between the Yangtze craton to the south (now part of the South China block), and the Sino-Korean craton to the north (now part of the North China block). From west to east, it comprises the Qinling, Tongbai, Hong'an, and Dabie Shan. The Sulu region, about 500 kilometers northeast of the Dabie and

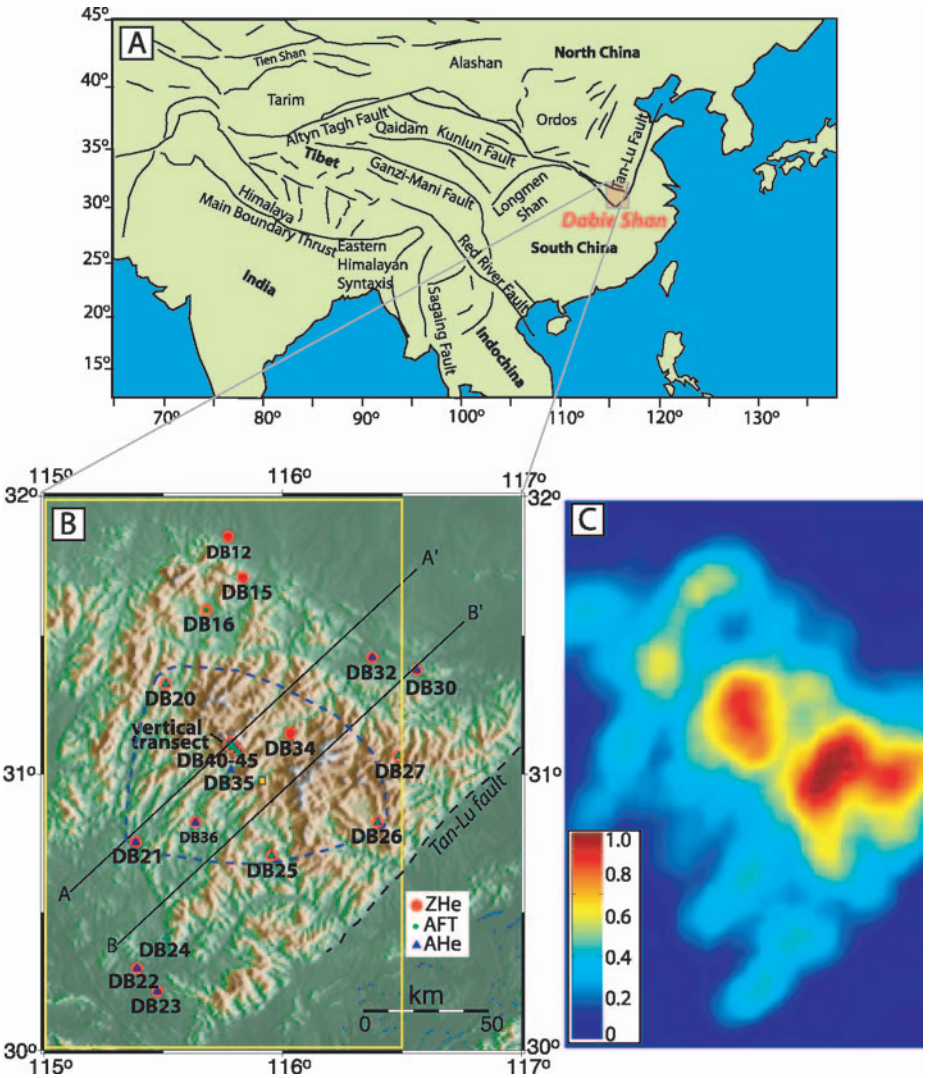

Fig. 1. **A.** Generalized tectonic map of part of southeast Asia, showing major active faults (black lines), mountain ranges, and location of the Dabie Shan (after Wang and others, 2001). **B.** Digital elevation model of the Dabie Shan region, and sample locations. Black lines are locations of cross-range profiles onto which sample data have been orthogonally projected in figures 2 and 4. Dashed blue line delineates samples from the core and flanks of the range, as referred to in text. Yellow square is location of central point used to reference radial distance of samples in figures 2 and 5. **C.** Mean elevation (km above sea level) for a 10-km window, for yellow boxed region in (B), used for closure depth calculations for the AHe system.

separated from it by the Tan-Lu fault, is interpreted to be an eastern extension of this belt. Yin and Nie (1993) proposed that the originally irregular margin of the Yangtze craton block may be responsible for the apparent separation between the Dabie and Sulu areas.

A variety of geochronologic and sedimentologic evidence points to a Triassic age for the initial cratonal collision, with metamorphism continuing into the Jurassic (Nie and others, 1994; Hacker and others, 1996). High- and ultrahigh-pressure (UHP) supracrustal rocks are thought to have been exhumed from depths as great as 120 to

140 kilometers (or higher; Zhang and others, 1999) near the end of the Triassic-Jurassic orogenic event (Hacker and others, 1996; Liou and others, 1996), to depths corresponding to ~200°C by the middle Jurassic (Hacker and others, 2000). Evidence for collision and rapid initial exhumation during the Triassic-Jurassic comes in part from zircon U/Pb ages throughout the Dabie Shan that are ~210 to 240 Ma, (although Proterozoic upper intercepts or cores are common) (Rowley and others, 1997; Hacker and others, 1998, 2000), as well as from white mica and biotite $^{40}Ar/^{39}Ar$ ages between about 280 to 118 Ma (Okay and others, 1993; Eide and others, 1994; Hacker and Wang, 1995; Hacker and others, 2000; Ratschbacher and others, 2000).

In the early to middle Cretaceous, the Dabie Shan experienced a second major orogenic event, as did many other regions in eastern China, that was dominantly extensional and accompanied by voluminous magmatism. This event was probably related to subduction of the paleo-Pacific plate to the east (Ratschbacher and others, 2000). Cretaceous plutons and orthogneisses with crystallization ages of 137 to 125 Ma (Xue and others, 1997; Ratschbacher and others, 2000) and estimated emplacement pressures of 4 to 9 kbar comprise almost half of the presently exposed rocks in the Dabie Shan. Assuming an average depth of 18 kilometers for these plutons (Ratschbacher and others, 2000), the time-averaged exhumation rate since their average crystallization age (133 Ma) would be about 0.14 km/myr. Ductile and brittle extensional deformation during and subsequent to the Cretaceous magmatism also resulted in exhumation of high-pressure and ultra-high-pressure coesite-diamond bearing rocks from about 18 to 30 kilometers depths to shallow crustal depths (Eide and others, 1994; Webb and others, 1999; Ratschbacher and others, 2000), although it is unclear if UHP rocks were already at the surface prior to the Cretaceous orogeny. Feldspar $^{40}Ar/^{39}Ar$ dating and petrologic and structural evidence indicate that the Northern Orthogneiss unit in the northern part of the range developed a broad domal structure at this time. $^{40}Ar/^{39}Ar$ cooling models of K-feldspar indicate that rocks now at the surface cooled through temperatures of approximately 200°C between ~200 to 90 Ma. Some of these K-feldspar ages are interpreted as cooling from re-heating between 110 to 90 Ma, and as late as 75 Ma in the nearby Tongbai region (Webb and others, 1999; Ratschbacher and others, 2000).

Although both the Triassic-Jurassic and Cretaceous orogenic events may have been responsible for most of the exhumation of the currently exposed UHP rocks in the Dabie, evidence for the timing of first exposure of UHP rocks at the earth's surface in this range is ambiguous (Xue and others, 1996; Ratschbacher and others, 2000). Grimmer and others (2003) addressed this by measuring $^{207}Pb/^{206}Pb$ and $^{40}Ar/^{39}Ar$ ages of detrital zircon and white mica, respectively, in synorogenic Triassic-Jurassic foreland sedimentary rocks surrounding the Hong'an-Dabie. They showed that the Hong'an-Dabie was the dominant sediment source, and they found two Triassic zircons and a few high-Si phengites in the Mesozoic sedimentary rocks. On this basis, they tentatively suggested that UHP rocks in the Dabie may have been exposed as early as the Middle Jurassic (190-160 Ma).

Cenozoic tectonic activity in the Dabie Shan has been inferred from geomorphic and kinematic evidence of Tertiary motion along large strike-slip and normal faults surrounding it and the Qinling Shan to the west (Peltzer and others, 1985; Ratschbacher and others, 2000), as well as from fault-proximal basins filled by Tertiary sediments. Ratschbacher and others (2000) estimated a total Tertiary exhumation from the Dabie Shan ≤5 kilometers, which is similar to the depth of Eocene sediments in the proximal basins east of the Dabie Shan. Part of the significance of this potential Tertiary exhumation derives from the possible influence of far-field and regional Tertiary tectonic events on the Dabie Shan, such as the Indo-Asian collision to the southwest (for example, Molnar and Tapponnier, 1975; Grimmer and others, 2002),

strike-slip-dominated escape tectonics to the south (for example, Tapponnier and Molnar, 1977; Tapponnier and others, 1986), and extensional deformation to the north (Peltzer and others, 1985). The question of orogenic reactivation of the range over its >200 myr history may also provide insight into the relationships between long-term exhumation rates, multiple orogenic pulses, and UHP rock exhumation (Xue-Cheng and others, 2003). Finally, the Cenozoic evolution of the Dabie Shan may also provide constraints on the problem of long-term maintenance of topographic relief in ancient orogens (for example, Pazzaglia and Brandon, 1996; Baldwin and others, 2003).

The only previous low-temperature thermochronologic constraints on the Dabie Shan come from a recent apatite fission-track dating study by Grimmer and others (2002) of the eastern Dabie and adjacent foreland basin. The range of AFT ages reported is 42 to 158 Ma, but most samples have ages of 55 to 90 Ma, attributed to gradual cooling from mid-Cretaceous heating. Eight samples, most of which are from near the Tan-Lu fault on the eastern boundary of the range however, have AFT ages between 42 and 55 Ma. Grimmer and others (2002) interpreted this as evidence for Eocene reactivation of the Tan-Lu fault zone and exhumation in the eastern Dabie; possibly a far-field effect of the Indo-Asian collision. However, none of the track length models of any of the samples in that study clearly require increased cooling rates since the Cretaceous. Although Grimmer and others (2002) interpreted track length models of a small number of samples as suggesting increased cooling rates in the Eocene, constant cooling rates since at least the late Cretaceous (in most cases mid-Cretaceous) provide suitable "good-fit" models to all the track-length data. In the present study, although we identify spatially variable cooling and exhumation rates in the Dabie Shan, we find no clear evidence for temporal variations in cooling rates since the Cretaceous. Furthermore, even if temporal changes in cooling rates did occur in the Dabie Shan (and elsewhere), they could not be convincingly demonstrated by only regional ages from a single system. This requires either topographically-controlled vertical transects of ages, or ages from multiple systems with different closure temperatures, both of which are presented here.

METHODS AND SAMPLES

We measured (U-Th)/He ages of apatite and zircon and fission-track ages of apatite in twenty-two individual samples from the Dabie Shan, although not all systems were measured on every sample. Numerous studies have established the utility of apatite (U-Th)/He dating, and its approximate closure temperature (for common cooling rates and crystal sizes) of 65° to 70°C (Wolf and others, 1996; Farley, 2000). Similarly, the basis and utility of apatite fission-track dating are well established, as is the closure temperature of about 110°C, for typical apatite compositions and cooling rates (for example, Gallagher and others, 1998).

Zircon (U-Th)/He thermochronometry has only recently been applied to tectonic studies, but both He diffusion experiments and age comparisons with other systems in slowly-cooled rocks suggest a closure temperature in the range of 160° to 200°C (Reiners and others, 2002). In particular, comparisons between zircon He ages and cooling trends derived from multi-domain diffusion models of K-feldspar $^{40}Ar/^{39}Ar$ dating support a zircon He closure temperature in this range (Kirby and others, 2002; Reiners and Spell, 2002; Reiners and others, unpublished data). In this study, we assume diffusion characteristics for He in zircon and ZHe closure temperature based on recent diffusion experiments at Yale that are consistent with previous results (Reiners and others, 2002); and are described in detail in a forthcoming study (Reiners and others, unpublished data; a subset are also described in Reiners and Spell, 2002). These step-heating experiments were performed on both rapidly cooled Cretaceous zircons with cooling and crystallization ages (100-150 Ma), U concentrations (~100-

400 ppm), and dimensions (50-60 μm tetragonal prism radii) similar to Dabie Shan zircons of this study, as well as on interior fragments of undamaged gem-quality zircons. Results from both types of specimens are essentially the same and indicate an activation energy (E_a) of 40 ± 1 kcal/mol, and a frequency factor (D_0) of 0.6 cm^2/s for He diffusion in zircon. These characteristics yield a closure temperature of 180°C for cooling rate of 10°C/myr and crystal size of 60 μm. Therefore, in subsequent interpretations requiring assumptions of zircon (U-Th)/He closure temperature, we assume a nominal closure temperature of 180° ± 20°C for ZHe.

Our samples (fig. 1) were collected from elevations between 32 and 1730 meters above sea level in the Dabie Shan, encompassing the full range of relief. Most samples were collected to provide broad areal coverage, but six samples were collected in a ~1.4-kilometer vertical transect (over a horizontal distance of ~5-6 km) from near the center of the range where the relief is highest. Most samples are from Cretaceous granitic and orthogneissic rocks originally emplaced or metamorphosed at ~12-25 kilometers depth. The remaining samples were collected from Carboniferous metasandstone (sample DB15), and Jurassic or Cretaceous sandstones (samples DB12, DB30, DB32). All ages reported here are interpreted as cooling ages of bedrock from which the samples were derived. Stratigraphic reconstructions suggest that the Jurassic/Cretaceous sandstones were buried beneath approximately 6 kilometers of sedimentary rocks (Xue and Jin, 2001), so even ZHe ages of these samples probably represent *in-situ* cooling ages, rather than unreset or partially reset cooling ages of their source(s).

RESULTS

In the following discussions, we distinguish between samples from the flanks of the range and core of the range (fig. 1), by referring to samples as either range-flanks, or range-core samples. Although this spatial classification coincides roughly with the geographic location of samples with respect to the mean topographic center of the Dabie Shan (and range-core samples are from areas with 50-km-averaged mean elevations >300 m, except for samples DB21 and DB27), the distinction between range-flank and range-core is made primarily on the basis of ages, not structural or rigorous topographic differences between the central and outer part of the Dabie.

ZHe ages throughout the orogen (table 1) are 76 to 155 Ma, and show an overall increase in age with distance from the center of the range (fig. 2). ZHe ages from range-flank samples are 114 to 155 Ma (with one exception at 88 Ma), whereas those from the range-core are 76 to 115 Ma (figs. 2 and 3). The oldest ZHe age, equal to 155 Ma is found in the northwestern corner of the range, even though in the cross-range transect it appears to be close to the range-core (fig. 2). ZHe ages in the vertical transect in the range-core increase from 76 Ma at 388 meters, to 112 Ma at 1730 meters, but the four highest samples (860 to 1730 m) are indistinguishable within error at 110 to 112 Ma. Below 860 meters, ZHe ages decrease rapidly with elevation, with a slope of 0.015 (+0.002/-0.003, 2σ) km/myr (R^2 = 0.95) (fig. 3). Slopes of age-elevation relationships for ZHe and other systems were estimated using weighted regression with the cooling ages as the dependent variable and the weights set using the errors for the ages. The estimated slope and uncertainties were then inverted to give the estimated exhumation rate and uncertainties.

AFT ages range from 44 to 86 Ma throughout the orogen (table 2). There are too few AFT data to resolve the flanks-to-core younging seen in the ZHe and AHe. The oldest AFT age (86 Ma) is from the most distal sample, in the far northwest corner of the range, which also has the oldest ZHe age (155 Ma). AFT ages increase with elevation in the vertical transect, from 44 to 73 Ma (except for the uppermost two samples, which decrease from 73 and 70 Ma with height), with a slope of 0.048 (+0.007/-0.009) km/myr (R^2 = 0.92).

AHe ages range from 24 to 66 Ma throughout the orogen, and, similar to ZHe, show a general younging towards the core of the range, where samples have AHe ages of 24 to 44 Ma, compared with 44 to 66 Ma for range flanks samples. Samples from the vertical transect span the entire range of range-core ages (24-44 Ma), and show a positive age-elevation correlation ($R^2 = 0.83$), with a slope of 0.070 ± 0.004 km/myr.

DISCUSSION

Cross-Range Exhumation Rate Gradient

Previous K-feldspar $^{40}Ar/^{39}Ar$ cooling models for Dabie Shan samples indicate final cooling through ~200°C at ~90 to 150 Ma (Hacker and others, 2000; Ratschbacher and others, 2000), with some samples from Hong'an Shan west of the Dabie Shan indicating younger ages of 75 to 85 Ma (Webb and others, 1999). Our ZHe ages of 76 to 155 Ma are broadly consistent with these results, given a ZHe closure temperature of 180° ± 20°C (Reiners and others, 2002; Reiners and Spell, 2002). The overall increase in ZHe ages away from the center of the range is also similar to previous observations of roughly concentric patterns in apparent reheating ages (above about 200°C) from K-feldspar thermochronometry, and inferred depths of exhumation (Hacker and others, 1996).

The concentric pattern of K-feldspar cooling ages has been interpreted as resulting from a mid-Cretaceous thermal dome with the ~200°C isotherm oblique to the present-day exposure level (Ratschbacher and others, 2000). To produce the spatial-temporal pattern observed in both the K-feldspar Ar ages and ZHe ages, these isotherms would have to have migrated towards the core over ~50 myr, at ~2 km/myr. An alternative interpretation is that ages young towards the core simply because exhumation rates have been higher there. The flank-to-core exhumation rate gradient would have existed through most of the Cretaceous to produce the 75 to 155 Ma ZHe ages observed across the range, and perhaps into the Tertiary, to produce the similar pattern of roughly concentric AHe ages, from 24 to 66 Ma from core-to-flanks.

To evaluate the hypothesis that there is a large-scale gradient in exhumation rates across the range, we need to estimate local exhumation rates from the age of each sample. In principle, this means simply dividing the closure depths by the measured cooling ages. However, closure depth for each sample is itself a function of exhumation rate, even in steady-state, since closure temperature is function of cooling rate. In addition, variations between measured ages are a function of not only differences in exhumation rates, but also differences in sample elevations with respect to the closure depth. One possible approach to account for these effects would be to first correct measured ages to those that would be observed at the mean local elevation (to account for differences in depth of the closure isotherm) using an assumed exhumation rate determined from the vertical transect (0.07 km/myr, or lower, as discussed below). Closure depth could also be determined from geotherms and cooling rates calculated from this assumed exhumation rate, and the ratio of closure depth to age would yield apparent local exhumation rate. This approach has the drawback of requiring an assumption of a single exhumation rate for samples suspected of having different exhumation rates. In addition, the apparent exhumation rate from the vertical transect is subject to some uncertainty because of short wavelength topographic effects, as described below.

Here we take an alternative approach, as outlined by Brandon and others (1998), for converting observed cooling ages to exhumation rates (for detailed description see Appendix A of Brandon and others, 1998). To estimate closure depth for each AHe age, we use a steady erosion model that relates closure temperature, depth, exhumation rate, and age as a function of the following parameters: pre-exhumational geothermal gradient (here assumed to be 20° or 25°C/km), thermal diffusivity (32

TABLE 1

Apatite and zircon (U-Th)/He data

Apatite sample	latitude	longitude	elev (masl)	method	corrected age (Ma)	± 2σ (Ma)	Ft	mwar (μm)	mass (μg)	U (ppm)	Th (ppm)	U/Th	He (nmol/g)
core													
DB20	31.19.625	115.30.649	207	furnace	33.0	2.0	0.79	71	77.1	19.6	55.0	0.36	4.59
DB25	30.42.342	115.57.245	231	furnace	37.4	2.2	0.82	86	93.0	3.61	12.1	0.30	1.09
DB26	30.49.626	116.23.863	334	furnace	37.6	2.3	0.68	44	12.1	26.1	63.6	0.41	5.66
DB21	30.45.327	115.23.102	108	laser	33.3	2.0	0.84	86	65.5	18.1	9.82	1.84	3.06
DB35	31.01.004	115.46.986	224	laser	31.7	1.9	0.80	72	77.2	22.3	17.1	1.30	3.60
DB36	30.49.505	115.38.101	238	laser	32.8	2.0	0.83	83	42.4	7.40	5.81	1.27	1.29
DB40	31.06.343	115.46.244	1729	laser/sg	43.4	2.6	0.74	49	3.8	27.5	29.0	0.95	5.92
DB41	31.06.475	115.46.736	1450	laser/sg	40.2	2.4	0.76	60	4.7	15.3	48.1	0.32	4.39
DB42	31.06.706	115.47.227	1070	laser/sg	33.9	2.0	0.75	54	4.9	17.5	82.6	0.21	5.06
DB43	31.05.804	115.47.324	860	laser/sg	37.7	2.3	0.83	77	16.5	10.4	26.5	0.39	2.79
DB44	31.05.146	115.48.525	620	laser/sg	34.9	2.1	0.77	59	6.4	14.9	58.5	0.25	4.16
DB45	31.04.406	115.49.396	340	laser/sg	25.3	1.5	0.77	60	4.3	8.52	2.20	0.26	0.949
DB45rep	31.04.406	115.49.396	340	laser/sg	22.5	1.4	0.73	49	2.9	10.5	3.50	0.33	1.01
flanks													
DB27	31.04.042	116.29.136	533	laser	61.8	3.7	0.67	43	24.0	8.85	67.1	0.13	5.56
DB24	30.24.725	115.30.779	31.7	furnace	45.2	2.7	0.74	57	29.0	7.52	31.6	0.24	2.72
DB22	30.17.864	115.23.397	116	laser	43.9	2.6	0.71	43	4.9	17.7	2.27	7.78	3.05
DB23	30.12.878	115.28.515	69.5	laser	63.9	3.8	0.70	45	30.5	23.4	71.3	0.33	9.68
DB30	31.22.571	116.33.631	209	laser	52.8	3.2	0.62	38	14.1	2.52	16.1	0.16	1.11
DB32	31.25.298	116.22.522	115	laser	65.5	3.9	0.72	50	56.0	10.3	58.8	0.18	6.15

TABLE 1
(continued)

Zircon sample	latitude	longitute	elev (m)	method	corrected age (Ma)	± 2σ (Ma)	Ft	mwar (μm)	mass (μg)	U (ppm)	Th (ppm)	U/Th	He (nmol/g)
core													
DB20	31,19.625	115,30.649	207	furnace	107	8.6	0.87	79	75.8	349	65.8	5.3	184
DB25	30,42.342	115,57.245	231	furnace	106	8.5	0.83	60	19.4	659	75.1	8.8	323
DB26	30,49.626	116,23.863	334	furnace	85.3	6.8	0.82	62	14.7	221	213	1.0	103
DB21	30,45.327	115,23.102	108	laser	96.3	7.7	0.84	63	2.45	366	46.7	7.8	166
DB36	30,49.505	115,38.101	238	laser	115	9.2	0.72	35	7.67	229	55.2	4.1	109
DB34	31,08.936	116,01.931	411	furnace	86.2	6.9	0.83	66	16.8	251	114	2.2	108
DB40	31,06.343	115,46.244	1729	laser	112	9.0	0.74	36	5.67	511	160	3.2	248
DB41	31,06.475	115,46.736	1450	laser/sg	110	8.8	0.79	44	10.9	439	114	3.8	218
DB42	31,06.706	115,47.227	1070	laser/sg	112	9.0	0.69	31	3.15	440	235	1.9	209
DB43	31,05.804	115,47.324	860	laser/sg	111	8.9	0.84	62	22.2	136	87	1.6	79.4
DB44	31,05.146	115,48.525	620	laser/sg	89.7	7.2	0.62	25	1.42	999	1672	0.6	418
DB45	31,04.406	115,49.396	340	laser	75.6	6.0	0.79	49	8.78	503	18.1	28	163
flanks													
DB27	31,04.042	116,29.136	533	laser	102	8.2	0.72	35	3.75	202	265	0.8	105
DB22	30,17.864	115,23.397	116	laser	137	11	0.77	41	5.69	173	81.9	2.1	107
DB23	30,12.878	115,28.515	69.5	laser	149	12	0.80	53	11.0	139	188	0.7	118
DB30	31,22.571	116,33.631	209	laser	114	9.1	0.85	73	27.0	44.2	26.1	1.7	26.5
DB32	31,25.298	116,22.522	115	laser	120	9.6	0.77	43	7.16	115	111	1.0	70.4
DB12	31,51.295	115,46.309	74.4	furnace	124	9.9	0.74	40	14.8	259	141	1.8	146
DB16	31,35.548	115,40.888	114	furnace	155	12	0.60	23	3.04	151	282	0.5	109
DB15	31,42.513	115,50.014	301	laser	87.7	7.0	0.78	48	7.72	618	417	1.5	266

Note: Ft is alpha-ejection correction (Farley, 2002); sg is single-grain analysis; mwar is mass-weighted average radius (or simply radius for single grains).

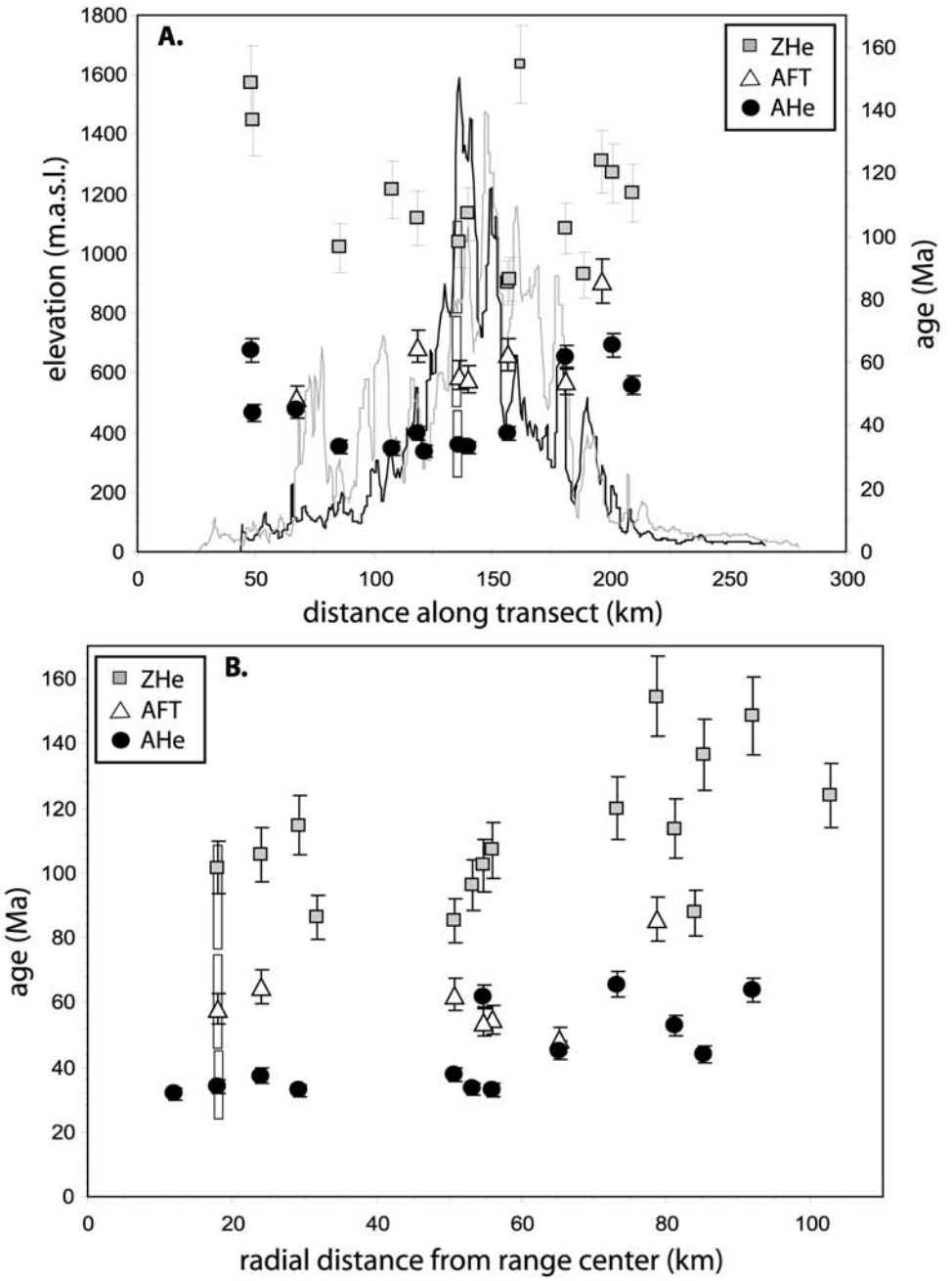

Fig. 2. **A.** Cross-range elevation (left y-axis) profiles along lines A-A′ (black) and B-B′ (grey) in figure 1, with He and fission-track ages (right y-axis) projected onto line B-B′. For the ZHe and AHe systems there is an overall decrease in cooling ages from flanks to core of the range. The most obvious exception to this is the oldest ZHe age (DB16); although this sample projects to near the core of the range, it is actually in the cluster of three ZHe samples far to the northwest of the core of the range seen in figure 1, and is shown here in a smaller symbol to distinguish it from the other samples. **B.** AHe, ZHe, and AFT ages as a function of radial distance from center of the range. In both A and B, the age of samples in the vetical transect is shown as the average age, and white boxes represent total range of ages. Error bars on (U-Th)/He ages are 2σ, those on AFT ages are 1σ.

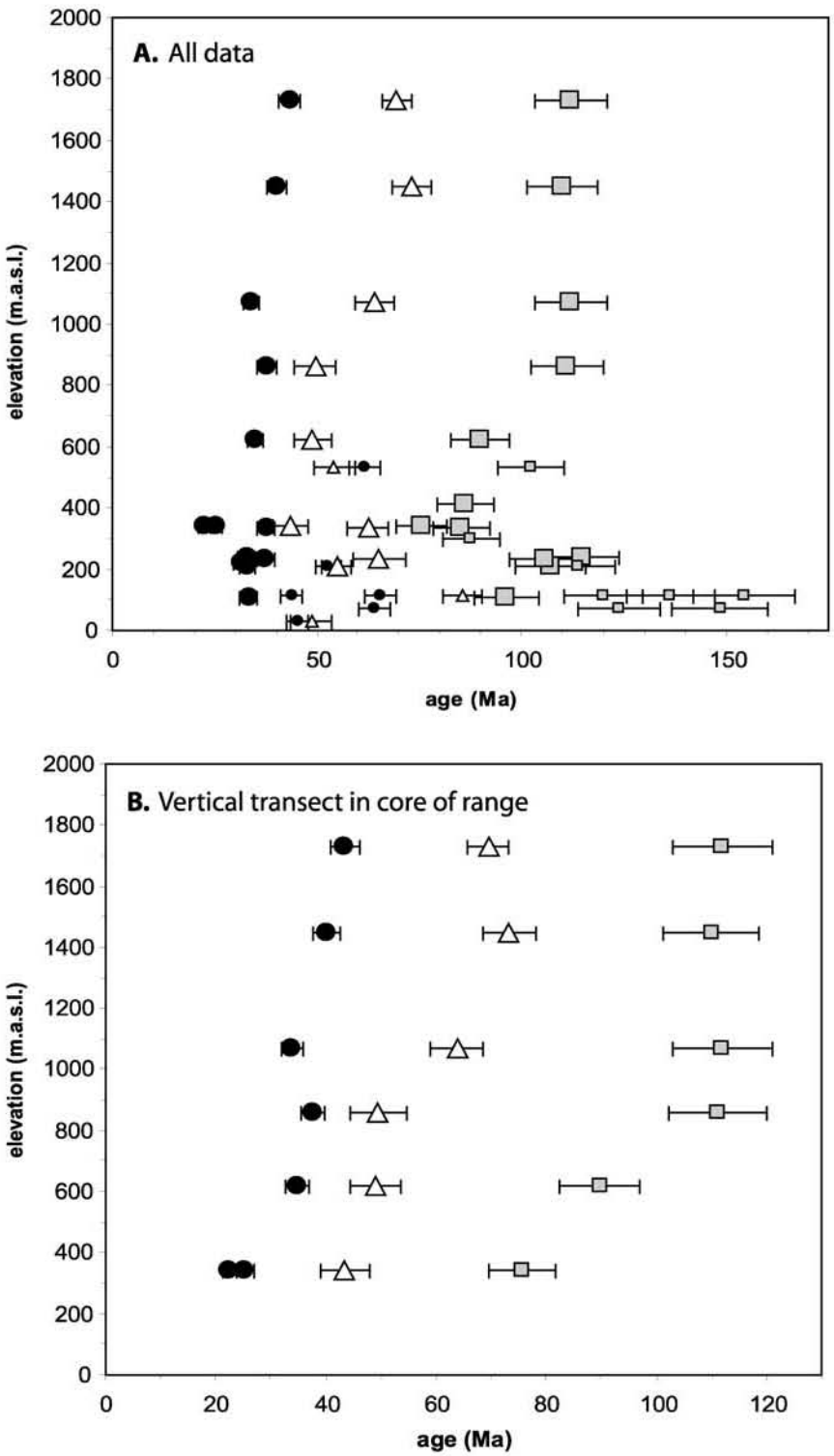

Fig. 3. **A.** Age-elevation plot for all data. Black circles: AHe; white triangles: AFT; grey squares: ZHe. Samples from the flanks of the range are shown as smaller size symbols. For the ZHe system, the range-flank samples show an inverse correlation with elevation, as expected from the general observation of increasing ages towards the lower-elevation range flanks. **B.** Age-elevation relationships (AER) for samples from the vertical transect (location in fig. 1).

TABLE 2

Apatite fission-track age and length data

Sample	ρ_s (10^6 tracks cm^{-2})	N_s (tracks)	ρ_i (10^6 tracks cm^{-2})	N_i (tracks)	ρ_d (10^6 tracks cm^{-2})	N_d (tracks)	Grains	Probability of Greater χ^2	Dpar (μm)	Dper (μm)	Pooled Age (Ma±1σ)	Mean Age (Ma±1σ)	Mean Track Length (μm±1σ) (tracks)
DB16	2.210	597	5.206	1406	3.569	4033	25	0.045	1.97	0.44	85.7±4.9	92.7±6.8	13.96±1.88 (145)
DB20	0.529	342	1.944	1258	3.558	4033	25	0.181	1.71	0.38	54.8±3.7	58.3±5.2	13.45±2.46 (143)
DB24	0.156	126	0.646	521	3.546	4033	25	0.316	1.52	0.37	48.6±5.0	51.2±6.0	13.09±2.28 (33)
DB25	0.126	154	0.387	473	3.534	4033	25	0.122	1.77	0.40	65.1±6.4	71.4±8.5	13.86±1.50 (85)
DB26	0.424	230	1.352	733	3.523	4033	25	0.057	1.79	0.33	62.6±5.1	71.3±6.7	13.93±1.97 (119)
DB27	0.160	167	0.588	614	3.511	4033	25	0.247	1.58	0.36	54.1±5.0	56.6±6.6	12.61±2.14 (28)
DB40	0.919	643	3.051	2134	4.073	4117	25	0.005	1.99	0.47	69.5±3.8	73.7±5.3	12.90±1.77 (107)
DB41	0.428	391	1.347	1230	4.068	4117	25	0.006	1.85	0.44	73.2±4.8	76.4±6.9	13.74±1.77 (101)
DB42	0.362	264	1.303	951	4.064	4117	25	0.016	1.87	0.47	63.9±4.8	76.3±11.5	13.25± 1.70 (105)
DB43	0.188	125	0.872	581	4.059	4117	24	0.211	1.74	0.46	49.5±5.1	52.2±6.2	13.04±1.59 (108)
DB44	0.252	152	1.182	714	4.054	4117	25	0.324	1.79	0.47	48.9±4.6	54.0±5.3	13.66±1.49 (101)
DB45	0.167	127	0.883	670	4.050	4117	22	0.042	1.87	0.49	43.5±4.4	47.4±6.6	13.58±1.68 (100)

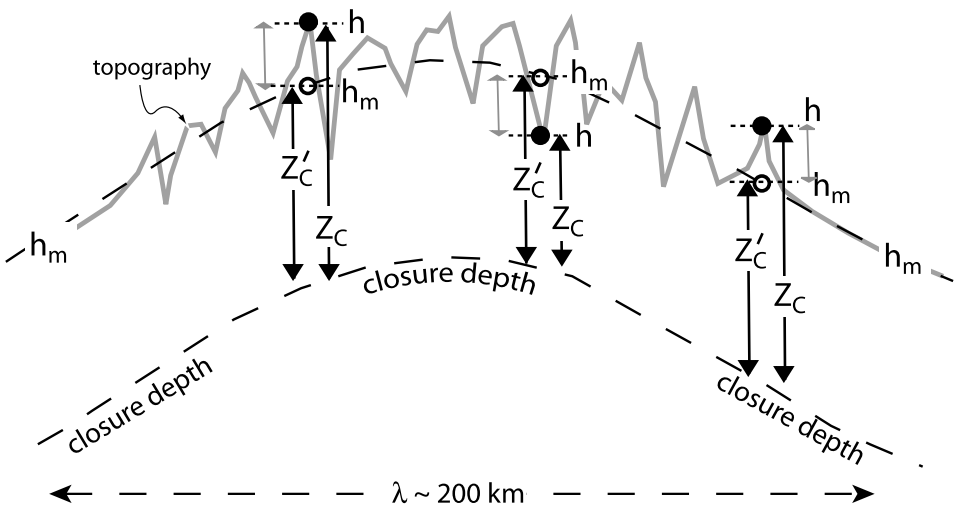

Fig. 4. Cartoon outlining method of calculating steady exhumation rates from AHe ages collected at different elevations in a mountain range with a long-wavelength (~200 km) topographic profile. Z'_c is the nominal depth to the closure isotherm, which, over long wavelengths (>~50 km), is parallel to the mean elevation of the mountain range h_m at any location. We used the method of Brandon and others (1998) to calculate effective closure temperatures and depths from observed AHe ages, assuming steady erosion rates. For these samples, the closure isotherm is about 52-55°C, which lies at about 1.3-1.9 km depth (for pre-exhumational geothermal gradients between 20-25°C and a mean annual surface temperature of 15°C). Samples are collected at different elevations h, so the effective vertical distance a sample has traveled since closure (total exhumation since closure) Z_c, is: $Z_c = Z'_c + (h - h_m)$. Elevation- and topography-corrected apparent exhumation rates for each sample (fig. 5) are then the ratio of Z_c and observed age.

km^2/myr), depth to constant temperature (30 km), and mean annual surface temperature (15°C) (fig. 4). For these calculations we also use He diffusion characteristics of apatite from Farley (2000), and an apatite radius of 60 microns (average for these samples). Values for geothermal gradient and thermal diffusivity are based on regional heat flow ranges from Hu and others (2000) and assumed thermal conductivity of ~2.5 W/mK, and are typical of many postorogenic continental settings and crustal rocks, respectively. The depth to constant temperature is roughly that of the Moho under the Dabie (30-35 km; Kern and others, 1999; Schmid and others, 2001; Xue-Cheng and others, 2003), and the surface temperature is a regional estimate for low- to intermediate-elevation regions of the Dabie. Since exhumation has probably been ongoing since at least the Cretaceous in the Dabie, it is difficult to identify a true pre-exhumational geothermal gradient. But this is not important here because post-Cretaceous exhumation rates are too slow to cause significant geothermal gradient variations with time. In other words, for the slow exhumation rates inferred from these data, the pre-exhumational and syn-exhumational geothermal gradients are essentially identical. Finally, this model requires the assumption of constant exhumation rate in a given location since movement of the sample through the closure depth. As shown in a subsequent section, interchronometer age differences, and age-elevation relationships in the vertical transect support the validity of this assumption.

Inferred AHe closure depths for samples in this study range from 1.63 to 1.85 kilometers for a geothermal gradient of 20°C/km, and 1.30 to 1.49 kilometers for a geothermal gradient of 25°C/km. These correspond to closure temperatures of 52° to 55°C, significantly lower than the typically cited nominal closure temperature for the AHe system (65°-70°C; Farley, 2000), because of the slow exhumation rates inferred from relatively old ages. This illustrates that simple assumptions of 65° to 70°C closure

temperatures and ~2 to 3 km closure depths for the AHe system can be 25 to 50 percent (or more) too high for slowly-cooled settings, even for typical geothermal gradients and crystal sizes such as these.

Because samples were collected at different elevations relative to the mean elevation of the long-wavelength topography, an elevation correction must be added to these inferred closure depths to derive total exhumation depths. Total exhumation for each sample is thus closure depth plus the difference between the sample collection elevation and the mean elevation (for a 10-km circle; see fig. 1C) of the sample collection region (fig. 4). Model exhumation rates for each sample are then the elevation-corrected closure depth divided by age. This steady-state model used to convert the AHe ages to exhumation rates does not correct for closure depth variations caused by topography with wavelengths shorter than that used to calculate mean topography (10 km). As shown in a subsequent section, for slow cooling rates such as these, two-dimensional topography with wavelengths less than 10 kilometers could potentially produce closure depth variations as high as 20 to 25 percent of the topographic relief within a 10 kilometer circle. With the exception of the vertical-transect samples, local (<10-km) topography around each of the samples in this study is less than ~500 meters, so the maximum variation of closure depth due to <10 kilometers wavelength topography would be about 125 meters, which is about 7 to 10 percent of the inferred closure depth discussed in the previous paragraph. Thus the fact that our model calculation here ignores the influence of short-wavelength topography may introduce errors in the estimated exhumation rates of about 7 to 10 percent. Moreover, this is a maximum error, because in general, real 3-D topography will not deflect topography as strongly as predicted by model calculations using 2-D topography.

Model exhumation rates determined from AHe ages of each sample using this method are shown in figure 5 as a function of distance across the range from SW to NE. Assuming a geothermal gradient of 20°C/km, rates increase from 0.025 to 0.058 km/myr from flanks to core, and assuming a gradient of 25°C/km, rates increase from about 0.020 to 0.047 km/myr. These data can be interpreted as a large (factor of 2-3) difference in long-term, Tertiary exhumation rates across the Dabie Shan, with the highest exhumation rates in the center of the range.

An alternative explanation for higher model exhumation rates in the core of the range is a recent increase in exhumation rates in the core of the range relative to the flanks, rather than a long-term difference across the range. This amounts to a decrease in the long-wavelength topographic relief of the range, as envisioned in models of Braun (2002a, 2002b). Several features of our data lead us to favor a model of spatially-varying but temporally-constant exhumation rates instead of a model of recent exhumation change in the core (recent-relief-reduction). First, we show in a subsequent section that the age-elevation relationship of the vertical transect in the range-core suggests a near-constant exhumation rate in this location since the Cretaceous through at least the mid-Tertiary, at a rate that is consistent with rates determined for other samples in the core of the range. Furthermore, extrapolation of this AHe age-elevation relationship in the vertical transect yields a zero-age intercept at a depth of ~1.2 kilometers below sea level. Adding the 0.7 kilometer mean elevation of the vertical transect to this yields the mean depth below the earth's surface for the zero-age intercept for the AHe system: 1.9 kilometers. This depth is precisely the inferred depth of closure for a steady exhumation rate of 0.06 km/myr, geothermal gradient of 20°C/km, and AHe age of 32 Ma (the average at the mean elevation of the vertical transect), suggesting steady exhumation has prevailed to the present. Second, the relief-reduction model would imply that exhumation rates across the range were constant until sometime after ~24 Ma, at which time the core of the range began

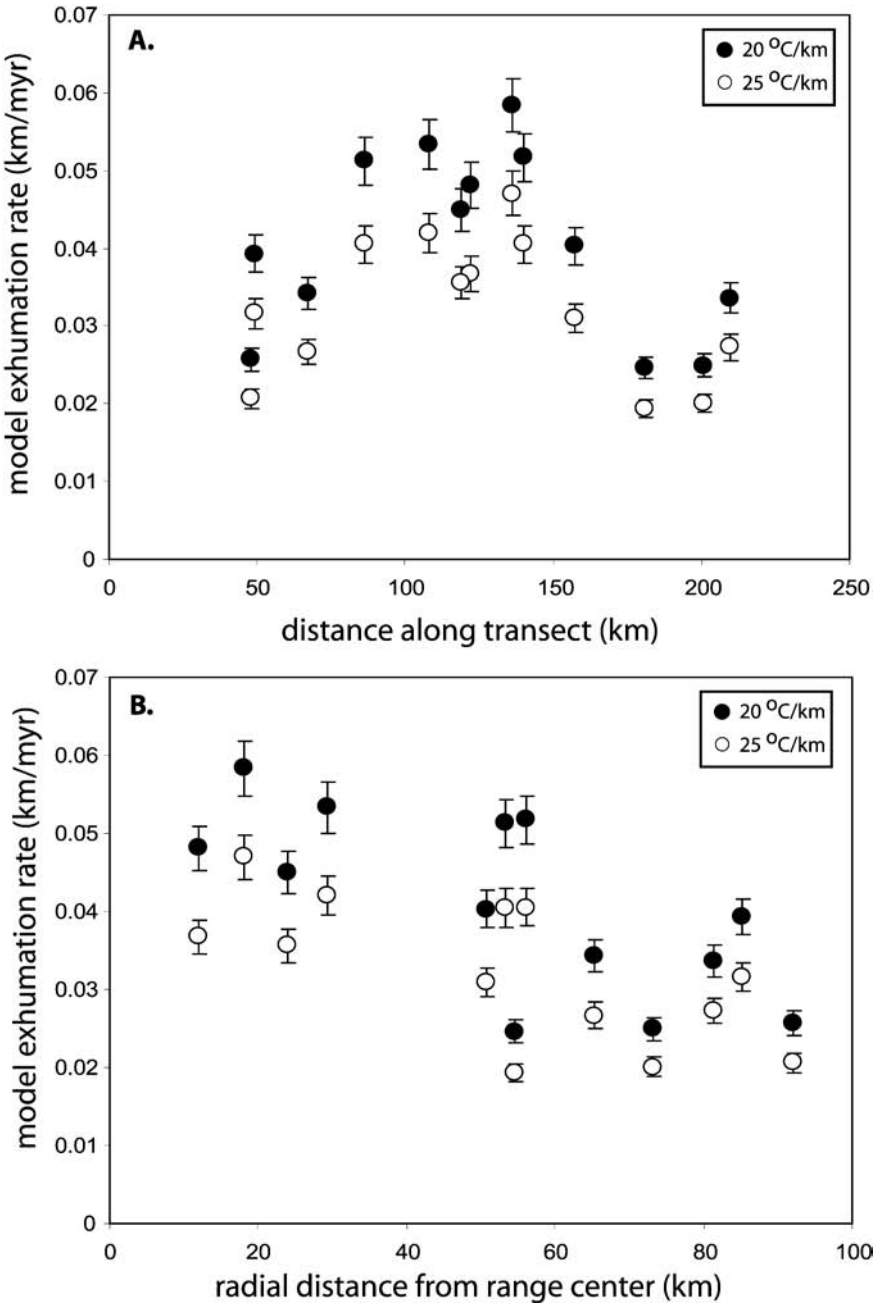

Fig. 5. Apparent average exhumation rates from observed AHe ages, across the Dabie Shan for time interval since each AHe age (23-44 Ma) as a function of distance across the range in the same transect as in figure 2 (**A.**), or radial distance from the center of the range (**B.**). Apparent rates are shown for assumptions of geothermal gradients of 20° and 25°C. The vertical transect samples are represented by a single age (31.7 Ma) corresponding to the age of the regression through the vertical transect AHe data at the mean elevation of that location (0.8 km). This location is the highest apparent exhumation rate in the range (0.058 km/myr for a geothermal gradient of 20°C/km, or 0.047 km/myr for a geothermal gradient of 25°C/km). Note that this is slower than the apparent exhumation rate from regression of the AER through the vertical transect itself (0.07 km/myr), although it is similar to the topography-corrected exhumation rate of 0.044-0.049 km/myr (fig. 7; see text for discussion). There is an overall increase in apparent exhumation rates from the flanks to core of the range, over a factor of about two to three.

exhuming several times faster than the flanks. This implies significantly higher topographic relief yet constant exhumation rates across the Dabie Shan prior to the ~24 Ma, counter to expectations that a decaying mountain range would erode faster in the high-elevation and high-relief regions. Finally, although not as clear as for AHe, the ZHe system also shows a similar flanks-to-core age variation, and there is a suggestion of such a trend for the AFT system as well. This spatial gradient in exhumation rates for the ZHe system could not be produced by a recent decrease in relief, since differences in ZHe ages are set much deeper than AHe (~6-8 km as opposed to ~1.5-2.0 km), and would require unreasonable extents and rates of recent exhumation, especially if restricted to more recently than 24 Ma. Thus we contend that the cross-range age gradient in ZHe may also be due to a long-term exhumation rate gradient, though we cannot apply a rigorous quantitative steady exhumation rate model to the ZHe ages because of the evidence for rapidly changing cooling rates at 90 to 120 Ma.

At least one testable prediction of our model for a long-term exhumation rate gradient across the Dabie Shan is that vertical transects on the flanks of the range should show not only older AHe ages, but also lower slopes of age-elevation relationships. It would be more difficult to collect long vertical transects in range-flank regions, because of their generally low relief, but shorter transects may be possible.

In summary, the spatial variation in AHe ages across the Dabie Shan reflects variation in long-term exhumation rates across the range, with the range-core eroding at a rate 2 to 3 times faster than the range-flanks, throughout the Tertiary, and possibly since the Cretaceous. Although it may be expected that the cores of post-orogenic mountain ranges would be eroding faster than the flanks, if topography is indeed decaying, we know of few if any observations such as these that have actually quantified the phenomenon.

Age-Elevation Relationships and Exhumation Rates

Whereas spatial variations in exhumation rates reflect different cooling ages across the range, temporal variations in exhumation rate are recorded in the age-elevation relationship (AER) of the vertical transect in the core of the range. To a first order, slopes of the AER for each thermochronometer record the vertical velocity of samples relative to the relevant closure isotherm. Deriving robust estimates of exhumation rates through time from these AERs, however, requires an assessment of the degree to which closure isotherm depths were spatially or temporally variable during exhumation, primarily because of potential complications from advective or topographic effects.

Outside of magmatic effects (no magmatic rocks younger than ~125 Ma are known from the Dabie Shan), the most commonly cited potential cause of temporal variations in geothermal gradients is high and transient exhumation rates. Thermal transients can be safely ignored however, if they arise from transients in exhumation rates that are less than about 0.1 mm/yr (Peclet number ~0.2). With the exception of the near-vertical upper part of the ZHe AER, the highest exhumation rate from the Dabie Shan AERs is several times lower than this, suggesting dominantly conductive control on heat transfer in the shallow crust since about 110 Ma.

A more important issue with the interpretation of AER slopes is topographic bending of near surface isotherms (Stüwe and others, 1994; Mancktelow and Grasemann, 1997; House and others, 1998, 2001; Stüwe and Hintermüller, 2000; Ehlers and others, 2001; Braun, 2002a, 2002b; Ehlers and Farley, 2003). Thermal gradients at temperatures below about 100°C in the upper crust can be significantly increased under valleys and depressed under ridges. This can lead to overestimation of exhumation rates from AERs because of the depth difference between thermochronometric closure of samples emerging at different elevations. Potential overestimation of exhumation rates from "vertical" transects is most significant for those thermochronom-

eters with the lowest closure temperature, and for long wavelength topography (for example, Stüwe and others, 1994).

The effect of topographic bending of isotherms in the upper crust is widely recognized (for example, Turcotte and Schubert, 1982), and has been used to provide minimum ages of topography and the evolution of paleorelief (House and others, 1998, 2001; Braun, 2002a, 2002b). More commonly, topographic effects are considered because of their complicating effects on interpretations of exhumation rates from low-temperature thermochronometric data. Two- and three-dimensional thermal models have also been devised to quantify such topographic influences (Stüwe and others, 1994; Mancktelow and Grasemann, 1997; Stüwe and Hintermüller, 2000; Ehlers and others, 2001; House and others, 1998, 2001; Braun, 2002a, 2002b; Ehlers and Farley, 2003).

Here we address a common problem related to topographic effects on age-elevation data in vertical transects, without involving sophisticated thermal models. There are essentially two questions: 1) if a vertical transect is collected over a given topographic profile with a characteristic wavelength, how much are closure isotherms bent by this topography, and 2) how much does this bending affect the apparent rate of exhumation from the AER? Stüwe and others (1994) addressed these questions for a variety of specific cases, including the effects of erosional exhumation, with an emphasis on the AFT system. We take a simplified approach, using a 2-D model of steady-state temperature distribution in the shallow crust underlying periodic topography of various wavelengths, following the methods of Turcotte and Schubert (1982, 2002, eqs 4-66) and Mancktelow and Grasemann (1997, eqs 25 and 26). Our model does not include the effects of erosional exhumation on crustal thermal structure because the very low Peclet numbers ($\sim$0.05-0.10) for these low exhumation rates would not significantly perturb isotherms from the static case.

We calculated the depth of 50° to 100°C isotherms beneath periodic topographic highs and lows (ridges and valleys), and then calculated the ratio of relief on these isotherms to relief of the topography, called the admittance ratio, α (Braun, 2002a). Braun introduced the admittance ratio in the context of a spectral analysis method for inverting low-T thermochronometric ages for changes in paleorelief (2002a); here we follow his notation but instead focus on the use of α for correcting topographic effects on age-elevation relationships. For an isotherm of a given temperature, α is a function of topographic wavelength, and is essentially zero at short wavelengths. Figure 6B shows this for the 50° to 100°C isotherms: at short wavelengths ($<\sim$ 5 km for 50-100°C), isotherms for temperatures above $\sim$50°C are essentially flat and unperturbed by topography ($\alpha \sim 0$). At long wavelengths, they are strongly bent by topography and follow it closely ($\alpha \sim$0.5-0.8). In this example, α reaches a maximum value of $\sim$0.8, regardless of temperature or wavelength, because of surface temperature differences in valley and ridge locations (atmospheric lapse rate = β; if $\beta = 0$, $\alpha \rightarrow 1$ at high wavelengths).

Examining the bending of isotherms by topography in this way has the advantage that the α is only slightly dependent on topographic amplitude (relief). At the relief in the region near the vertical transect in the Dabie Shan ($\sim$0.7 km, or one-half the distance from valley bottom to ridge top), topographic relief has a negligible effect on α at any wavelength. Thus figure 6B provides a convenient measure of how much an isotherm of interest (that is, a closure isotherm) is bent under topography of a specific wavelength of interest, regardless of topographic relief. For the present problem of evaluating the effect of topography on the AER of the AHe system in our vertical transect then, we need estimates for the temperature of the closure isotherm, as well as the wavelength of topography.

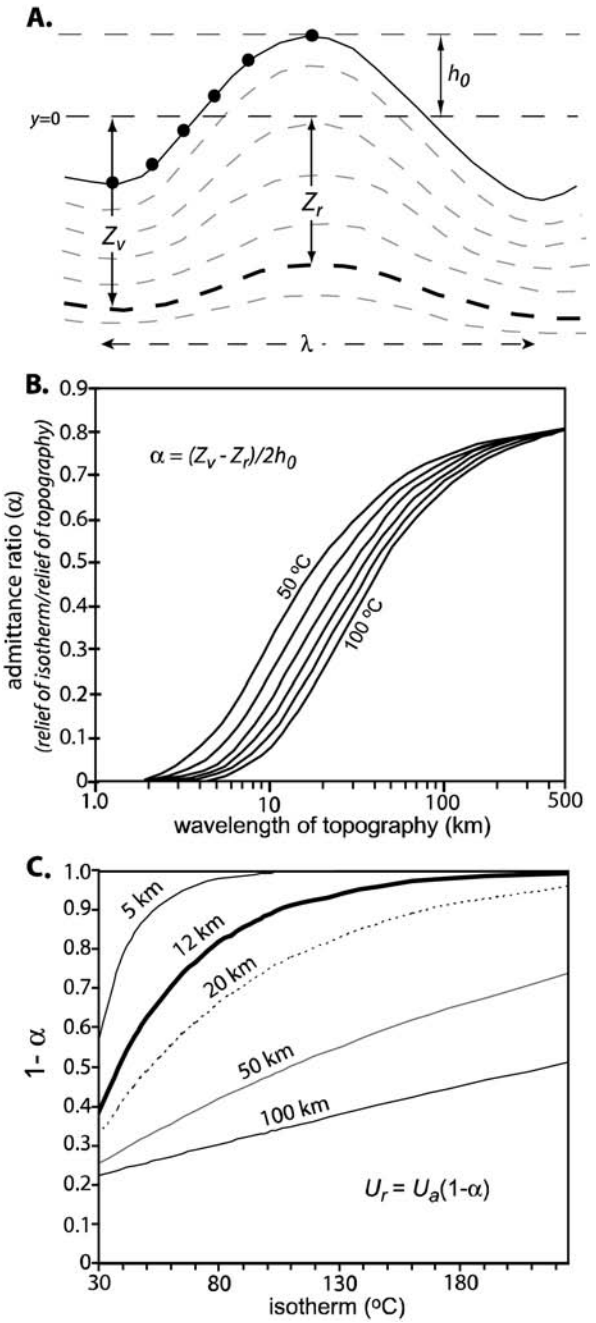

Fig. 6. **A.** Schematic illustration of the topographic influence on isotherms under a "vertical" transect used for constraining exhumation rates from thermochronometric ages. Samples are collected over λ/2, and relief of $2h_0$. Note that we specify $2h_0$ as the full topographic relief (rather than h_0, as some papers use); thus h_0 is amplitude of topographic relief, in agreement with typical use of the term in the context of a sine or cosine wave. Measured from a reference (mean) elevation ($y = 0$), the depth to the closure isotherm is greater under valleys (Z_v) than under ridges (Z_r). This difference decreases with depth and higher temperature isotherms, or, for a given temperature isotherm, with decreasing λ. For the vertical transect of samples in the core of the Dabie Shan, λ = 12 km and h_0 = 0.70 km (see text for discussion). **B.** The admittance ratio α, as a function of topographic wavelength. α is the ratio of relief on an isotherm to relief on

As shown above, assuming geothermal gradients of about 20° to 25°C and steady cooling, Tertiary exhumation rates for the range-core of the Dabie Shan are in the range of 0.05 to 0.07 km/myr. For the crystal sizes of these samples, this means that closure temperatures, and therefore closure isotherms of interest, are in the range of ~50° to 55°C. We approximate the topographic wavelength and amplitude for the vertical transect as those along the sampling transect, which is oriented approximately orthogonal to topographic grain. Although the real topography in the vicinity of the vertical transect is far from periodic infinite valleys and ridges, the transect was collected over a distance of about 6 kilometers, from the lowest point in a valley to the highest point at the top of a roughly symmetric peak with a general elongation to the northeast and southwest (fig. 1). Because the samples capture the entire range of elevation in this topography, we assume that the appropriate topographic wavelength for this problem is 12 kilometers (2 times the horizontal distance between lowest and highest samples).

Figure 6B shows that for a topographic wavelength of 12 kilometers, 50° to 55°C isotherms will be deflected beneath a 2-D valley and ridge by about 30 to 37 percent of the topographic relief (that is, $\alpha = 0.30\text{-}0.37$). It should be noted that this α estimate is based on a 2-D representation of topography, whereas real 3-D topography may be important to consider, especially in the absence of long parallel ridges (Stüwe and others, 1994; Stüwe and Hintermüller, 2000). In our case, assuming 2-D topography probably leads to overestimation of α, since the topography of the vertical transect is not an infinite ridge and is in fact more like a single peak, which has less isotherm bending "power." Thus this analysis provides a useful estimate of the likely maximum α, or maximum deflection of the closure isotherm under the topography of the vertical transect.

The next question we address is how much this admittance ratio (α) affects the apparent exhumation rate inferred from the AER of a vertical transect collected over this topography. Stüwe and others (1994) noted that the apparent exhumation rate from a vertical transect, can be simply related to the "model" exhumation rate (assuming steady-state and other conditions are also satisfied) by the relative amplitudes of topography and isotherms. Their analysis used a slightly different convention however, in which isotherm depth at any point was measured from the lowest point in the topography. If isotherm depth is instead measured from a reference height of local mean elevation, as in the Turcotte and Schubert (1982, 2002) and Mancktelow and Grasemann (1997) models, then "model" exhumation rate U_r, is equal to apparent exhumation rate U_a, multiplied by (1-α) (Braun, 2002a). This is the same result as that of Stüwe and others (1994), but the convenient correction factor for exhumation rates from vertical transects is more easily obtained by this approach, because α is largely independent of topographic relief. In our case, for $\alpha = 0.30\text{-}0.37$, and $\lambda = 12$ km, we find that model exhumation rate as measured by AHe ages for the vertical transect in

its overlying topography, $\alpha = (Z_v - Z_r)/2h_0$. For isotherms of about 50-70°C, topographic wavelengths greater than about 5 km produce significant relief on isotherms at depth and thus significantly influence apparent exhumation rates from AER of "vertical" transects. α does not exceed ~0.8 for any topographic wavelength in this example because of the effect of atmospheric lapse rate (4.5 K/km) on surface temperature differences beneath valleys and ridges (mean annual surface temperature is assumed to be 15°C in this example). Parameters used for these calculations are: surface radiogenic heat production: 1 μW m^{-3}; reduced heat flow: 45 mW m^{-1}; characteristic depth of heat production: 10 km; thermal conductivity: 2.4 W K^{-1}m^{-1}. **C.** The function (1-α), as a function of isotherm temperature. (1-α) is the factor applied to apparent exhumation rates U_a, to derive "real" exhumation rates U_r, from vertical transects to correct for topographic effects on isotherm depths (also see Braun, 2002a). This is the same as Stüwe and others's (1994) $U_r = U_a(\Delta z/h)$, but (1-α) is largely independent of topographic relief. For the case of $\lambda = 12$ km, and closure isotherm = 52-55°C, (1-α) is ~0.63-0.70. So the exhumation rate derived from the vertical transect in the core of the Dabie Shan is ~0.67 x (0.070 km/myr), or ~ 0.047 km/myr.

the core of the Dabie Shan is 0.63 to 0.70 times the apparent exhumation rate (fig. 6C). Thus the apparent exhumation rate since the mid-Eocene of 0.070 km/myr becomes a model exhumation rate of about 0.044 to 0.049 km/myr. This shows that apparent exhumation rates calculated from AHe vertical transects collected over distances as short as 6 kilometers could potentially require corrections as large as 30 to 40 percent.

We emphasize that the α estimated here is likely to be a maximum, because of 3-D topographic effects, so the model exhumation rate indicated by the AHe AER can be thought of as bracketed by a minimum of 0.05 km/myr (for maximum α) and maximum of 0.07 km/myr ($\alpha = 0$). Even with this maximum topographic correction however, the model exhumation rate from the vertical transect in the range-core is about 2 to 2.5 times faster than the exhumation rates estimated for the flanks of the range from steady-rate models discussed above. Finally, although it is well known that high exhumation rates can increase the topographic effect on AERs (for example, Stüwe and others, 1994; Mancktelow and Grasemann, 1997) as isotherms are "pushed" higher into the topography, this exercise shows that extremely *slow* exhumation rates can also enhance topographic effects on AERs, for a different reason. In such cases, slow cooling rates significantly decrease closure temperatures of minerals of interest, meaning effective closure isotherms are closer to the surface and more strongly affected by topography.

As suggested in figure 6, for a given topographic wavelength, apparent exhumation rates from AFT data in vertical transects are not as strongly affected by topography as rates from AHe data. For our case of 12 kilometers wavelength, the maximum α for a closure isotherm of about 100°C is less than about 0.1, so the apparent exhumation rate from AFT data in the vertical transect would be within 10 percent of that of the model exhumation rate, or ~0.042 to 0.047 km/myr since 44 to 70 Ma.

The topographic bending effect of 12 kilometers wavelength topography on the depth of the ~180°C isotherm is less than 5 percent (fig. 6C), so apparent exhumation rates from the ZHe data are not significantly affected by topography of the transect. However, as discussed above, the extremely rapid cooling before ~110 Ma implied by the essentially vertical AER for ZHe in the upper part of the vertical transect is difficult to relate directly to exhumation rates. Although this part of the transect could be interpreted as exhumation rates of at least 0.5 km/myr, it is quite possible that rates that fast, as well as previous events in the well-documented high-temperature Cretaceous orogeny, led to highly transient thermal effects, such as thermal relaxation following rapid exhumation, that prohibit accurate exhumation rate inferences. Subsequent to this rapid Cretaceous cooling (and perhaps rapid exhumation) however, cooling rates decreased, as the lower part of the ZHe AER and the AFT AER imply exhumation rates of only 0.015 and 0.048 km/myr, respectively.

Reconstructed Multi-Chronometer AER

To better constrain the timing and magnitude of exhumation rate changes in the core of the Dabie Shan, we constructed a composite vertical pseudo-transect using data from all three thermochronometers. Elevations of the AFT and ZHe ages were increased by an amount proportional to the difference between their closure temperatures and that of the AHe system. We used values based on estimates above, which give closure temperature differences of 40°C for AFT-AHe and 110°C for ZHe-AHe, and a geothermal gradient of 25°C/km to convert temperature to depth. This procedure allows all ages to be considered as representing cooling through the same closure temperature and closure depth (in effect, the same chronometer). As long as the thermal profile has remained stable since ~100 Ma, which is reasonable over the range of exhumation rates suggested by these data, this method does not depend on the actual closure temperatures of each system—only their differences. In this case, the reconstructed pseudo-AER provides an exhumational history for the Dabie Shan

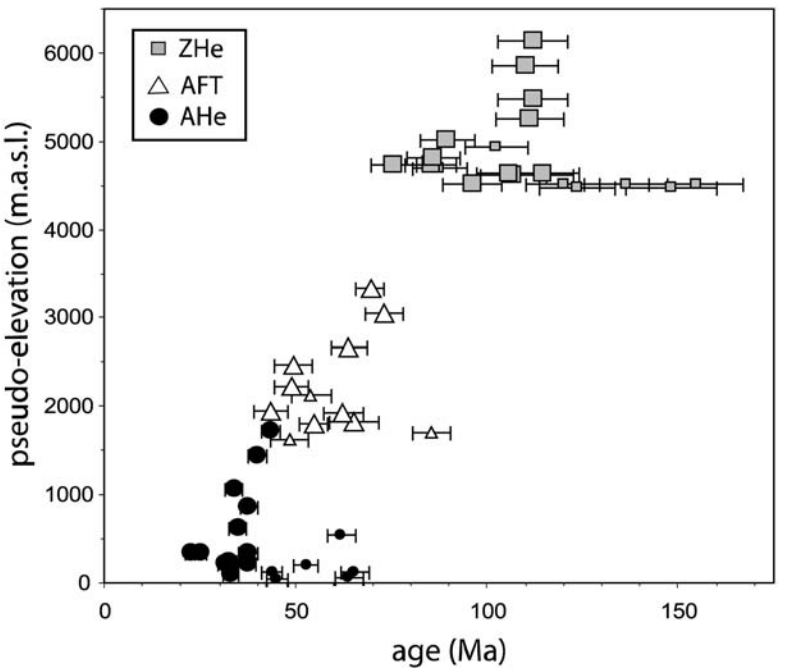

Fig. 7. Composite vertical pseudo-transect constructed from ages of all three chronometers, with elevations corrected in proportion to closure temperature difference with AHe. A geothermal gradient of 25°C/km was assumed. Closure temperature differences were assumed to be 40°C for AHe-AFT and 110°C for AHe-ZHe. Samples from the range flanks are shown as small symbols. The overall pattern of the composite pseudo-transect suggests a period of rapid cooling at about 110 Ma, followed by slower and relatively constant rates until at least 24 Ma, with possible minor changes. Symbols as in figure 2. Error bars on (U-Th)/He ages are 2σ, those on AFT ages are 1σ.

analogous to that of ~5 to 6 kilometers vertical transect for a single chronometer (fig. 7).

The vertical pseudo-AER (fig. 7) shows a pattern similar to that in many exhumed crustal sections (for example, Fitzgerald and others, 1995). Ages at the top of the section are nearly invariant with elevation, suggesting a pulse of rapid exhumation sometime before ~100 Ma, preserved in the structurally highest, or in this case, highest-temperature, samples of the range-core. At lower elevations, ages decrease strongly with decreasing elevation, suggesting lower exhumation rates after ~100 Ma. It is difficult to discern changes in slope in younger-aged samples in this plot, although it could be qualitatively suggested from figure 7 that there is a higher slope in the multichronometer trend (and therefore possibly an increased exhumation rate) between about 60 to 80 Ma, followed by slower rates through 25 to 30 Ma. More quantitative estimates of exhumation rate changes in this time require modeling approaches discussed below.

Model Long-Term Cooling and Exhumation Histories

Model cooling and exhumation rates through time in the Dabie Shan can be constrained more quantitatively by forward modeling (U-Th)/He and fission-track age evolution, for samples in the vertical transect, for time-temperature paths resulting from various exhumation histories. This can be done by essentially guessing an initial thermal history, and therefore exhumational history (assuming constant geothermal

gradients of 20-30°C), that yields a predicted age close to the observed age for the shallowest sample. This then predicts fixed cooling and exhumational histories for all other samples in the transect, as we assume that relative sample depths were constant and equivalent to modern elevation differences through time. Thermal/exhumational histories are then adjusted to produce a "best-fit" thermal history with good correspondence between observed and predicted ages for all systems at all elevations.

Regardless of regional exhumation rate, samples in the vertical transect cooled at different rates during exhumation through the upper 1 to 3 kilometers because of topographic bending of isotherms. Thus in order to avoid spurious effects in the model age trends for the lowest temperature systems (AHe and AFT), and to account for topographic effects in the final stage of cooling, the low-elevation samples must cool faster, and high-elevation samples slower. This effect is lessened to some degree by the atmospheric temperature lapse rate, which causes cooler present-day temperatures at higher elevation samples. We have combined these effects to account for both cooling through topography, and lapse rate, by assuming a final temperature of 15°C, less lapse rate (6 K/km) times elevation.

For the thermal and exhumational history of each sample we modeled AFT ages using a fission-track production-annealing model (AFTSolv; Ketcham and others, 2000) incorporating kinetic annealing parameters, and AHe and ZHe ages using a He production-diffusion model (after Wolf and others, 1998). As no model currently solves the inverse problem for combined He and fission-track ages (and track-lengths, for the latter), we tested several dozen candidate thermal histories using both codes to produce a "best-fit" thermal/exhumational history.

Figure 8 shows best-fit thermal histories and predicted ages for three cooling-history models, all involving cooling of a 1.4 kilometer vertical section of crust analogous to that of the vertical transect in the core of the range. All models share a common feature of relatively rapid cooling prior to 115 Ma, modeled here as 8° to 13°C/myr, or an exhumation rate of about 0.3 to 0.5 km/myr, although this model is not sensitive to this rate, and values several times higher could also satisfy the data. The ages and AERs of the AFT and AHe samples, as well as those of the lower elevation ZHe samples, are more sensitive to cooling rates subsequent to 115 Ma.

The first model (first row of fig. 8) shows that overall distribution of ages and AERs for all samples can be reproduced quite well by assuming constant exhumation rates (0.06 ± 0.01 km/myr) since 115 Ma. The only predicted ages falling more than 2σ outside of measured ages for this model are in the ZHe system (fig. 8C). The constant rate model fails to predict the strong curvature in the lower-elevation part of the ZHe AER. If model exhumation rates are strongly decreased after 115 Ma (that is, following the Cretaceous orogenic event) to until ~60 to 80 Ma, the curvature of the ZHe AER can be matched more precisely, as shown in the second and third rows of figure 8. Matching the inflection in the low elevation part of the ZHe AER requires holding exhumation close to zero until ~60 Ma (second row of fig. 8), when it increases to 0.12 to 0.19 km/myr until 40 Ma, and then decreases again until the present, at rates of 0.06 ± 0.01 km/myr as in the first model. This model provides a good fit for all data except for some of the higher elevation AFT ages, which are underpredicted by 12 to 22 myr. The fit to these AFT ages can be improved by invoking very slow exhumation rates from 80 to 60 Ma (0.01-0.02 km/myr), and a higher rate (0.06-0.09 km/myr) between 80 to 40 Ma, before returning to rates of 0.06 ± 0.01 km/myr since 40 Ma.

The most important general result of these forward models is that although small changes in exhumation rates after about 115 Ma can reproduce some minor features of the AERs from the core of the Dabie, models that invoke changing exhumation rates do not significantly improve the overall fit of predicted to observed ages relative to a constant rate model. Aside from evidence in the lower ZHe AER for relatively slow

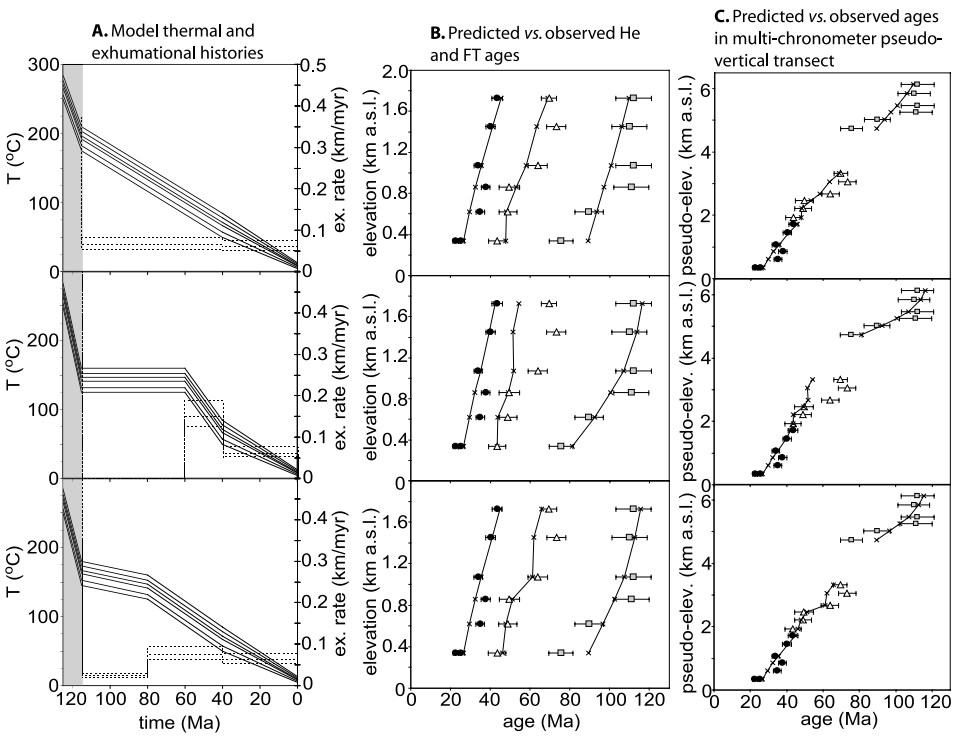

Fig. 8. Model thermal histories, exhumation rates, and predicted *versus* observed (U-Th)/He and fission-track ages for samples from the range-core vertical transect. Each row of plots represents thermal histories, exhumation rates, and predicted ages for a different exhumation model (see below, and text for discussion). **A.** Model thermal histories (solid lines and left y-axis) for samples of the range-core vertical transect, and corresponding exhumation rates (dashed line and right y-axis). Three different exhumation rates are shown in each model thermal history, corresponding to geothermal gradients of 20°, 25°, and 30°C/km (the highest rate at any time corresponds to the lowest geothermal gradient). Exhumation rates are calculated based on the thermal history of the sample with a present elevation of 860 meters above sea level (close to mean elevation of the vertical transect and topography in this location), so that the late-stage exhumation rates are not significantly affected by topographic and lapse rate effects on the post-40-Ma part of the thermal history. These thermal histories were chosen to predict cooling ages of all three systems shown in B and C, using a He diffusion-production model (after Wolf and others, 1998) and AFTSolv (Ketcham and others, 2000). Thermal histories prior to 115 Ma (the age of rapid cooling recorded by ZHe in the vertical transect) are poorly known, and could be significantly faster than shown here without affecting the predicted ZHe, AFT, and AHe ages shown in this model. This region of the plots in part A are shaded grey. **B.** Predicted ages (x's joined by black lines) and observed ages (other symbols) for samples from the vertical transect, for thermal histories shown in A. Fission-track production-annealing models use Dpar kinetic parameters measured on each sample (which are different for each sample, thus non-constant slopes for AFT AERs), and He production-diffusion models use He diffusion parameters from Farley (2000), apatite radius of 60 μm (average for these samples), and incorporate the effects of alpha ejection. **C.** Composite vertical pseudo-transect showing predicted versus observed ages of all chronometers (see text and fig. 6 caption for details of pseudo-transect construction). Error bars on (U-Th)/He ages are 2σ, those on AFT ages are 1σ. The first row of model results represents a thermal history of a constant cooling and exhumation rate (0.06 ± 0.01 km/myr) since 115 Ma. The second row represents constant temperature and no exhumation from 115-60 Ma, followed by relatively rapid cooling and exhumation (0.10-0.20 km/myr) from 60-40 Ma, and slow cooling and exhumation (0.06 ± 0.01 km/myr) until present. The third row is similar to the second model, except that 115 to 60 Ma cooling and exhumation rates are low (0.01-0.02 km/myr) but not zero, and 60 to 40 Ma rates are lower (0.06-0.09 km/myr). The first model (constant rates) is designed to illustrate the plausibility of a constant exhumation rate in reproducing the He and FT ages of the core of the Dabie Shan. The second model seeks primarily to match the inflection at low elevation in the ZHe AER by holding temperatures constant in the ZHe partial retention zone until 60 Ma, but this model underpredicts some of the high-elevation AFT ages. The third model seeks to improve the fit to the high-elevation AFT ages by allowing earlier cooling, but in doing so does not reproduce the youngest ZHe age at low elevation.

cooling immediately following high cooling rates of the mid-Cretaceous, there is little compelling evidence for exhumation rate changes after 115 Ma except perhaps modestly increased rates between 80 to 40 or 60 to 40 Ma (fig. 8A, two lower models). However, even in these models, exhumation rates of 0.06 ± 0.01 km/myr since ~40 Ma provide the best-fit to the AHe and AFT data (fig. 8).

The possible increased exhumation rates in the late Cretaceous through early Tertiary suggested by two of the models are consistent with a Dabie source for much of the 4.8 kilometers of sediment filling early Tertiary basins around the Dabie, as well as evidence for Tertiary faulting in the area (Peltzer and others, 1985; Ratschbacher and others, 2000). One potential cause for increased exhumation rates beginning ~50 Ma is far-field deformation from the Indo-Asian collision, ~1500 to 2000 kilometers to the west-southwest, as suggested by Grimmer and others (2002). However, at least one other study has noted that not all Late Cretaceous-Early Tertiary tectonic activity in southeast Asia is necessarily attributable to the Indo-Asian collision, but may instead be related to changes in Pacific-Eurasian plate motions at this time (Northrup and others, 1995). In any case, even if late Cretaceous through early Tertiary exhumation rates were higher than following the mid-Cretaceous event (which is not clearly required; fig. 8), they were quite modest in magnitude compared with those in the mid-Cretaceous (< 0.15 km/myr, compared with >0.5 km/myr).

More notable is the lack of evidence for an increase in exhumation rates beginning after 60 Ma. All three of the best-fit models in figure 8 involve either no change in exhumation rates, or a decrease in exhumation rates at 40 Ma. This contrasts with the interpretations of Grimmer and others (2002), who suggested an increase in cooling rates at 45 ± 10 Ma in the Dabie, based on several 40 to 55 Ma AFT ages. Although we observe a clustering of early to mid-Tertiary AHe ages in the core of the Dabie, by itself this does not constitute evidence for a discrete cooling or exhumation event at this time. In fact, relative AHe, AFT, and ZHe ages in the same samples, as well as AERs in the vertical transect of the core of the range, indicate relatively steady cooling and exhumation rates (~1.6 °C/myr, or 0.06 ± 0.01 km/myr) in the core of the Dabie since the Cretaceous.

The Eocene AFT ages of Grimmer and others (2002) were found within ~10 to 35 kilometers of the Tan-Lu fault, on the eastern border of the Dabie Shan, leading them to suggest Cenozoic reactivation of the Tan-Lu fault as a cause for some unspecified amount of tectonic exhumation. Among our samples, the one closest to the Tan-Lu fault (~20 km away; DB26) has the oldest AHe age among the range-core samples (36.7 Ma), aside from high-elevation samples of the vertical transect. Another nearby sample, 30 kilometers from the fault, also has an old AHe age, of 61.8 Ma. However, our sample locations are not well suited to addressing the question of younger ages towards the Tan-Lu fault, so we cannot rule out Tertiary tectonic exhumation at the eastern margin with any certainty.

Finally, the exhumational history of rocks in the core of the Dabie Shan can also be extended to the initial Triassic-Jurassic UHP metamorphism (fig. 9). Moderately well-constrained depth-time data can be derived from 1) 120 to 140 kilometer estimates of UHP metamorphism and U/Pb and Ar/Ar ages on high-temperature assemblages (Hacker and others, 2000), 2) Al-in-hornblende barometry (Ratschbacher and others, 2000) and zircon U/Pb ages (Hacker and others, 1998) on samples of the Cretaceous granites and orthogneisses, 3) assumptions of closure depths corresponding to cooling through inferred closure temperatures of 200°C for K-spar $^{40}Ar/^{39}Ar$ at 90 to 120 Ma (Ratschbacher and others, 2000), and 4) cooling ages and closure depths of the (U-Th)/He and fission-track systems (this study). Figure 9 shows that although exhumation rates in the Late Triassic and Jurassic were at least ~1 km/myr, rates over the last ~100 myr have been at least 10 to 20 times slower, and no more than about 5 to

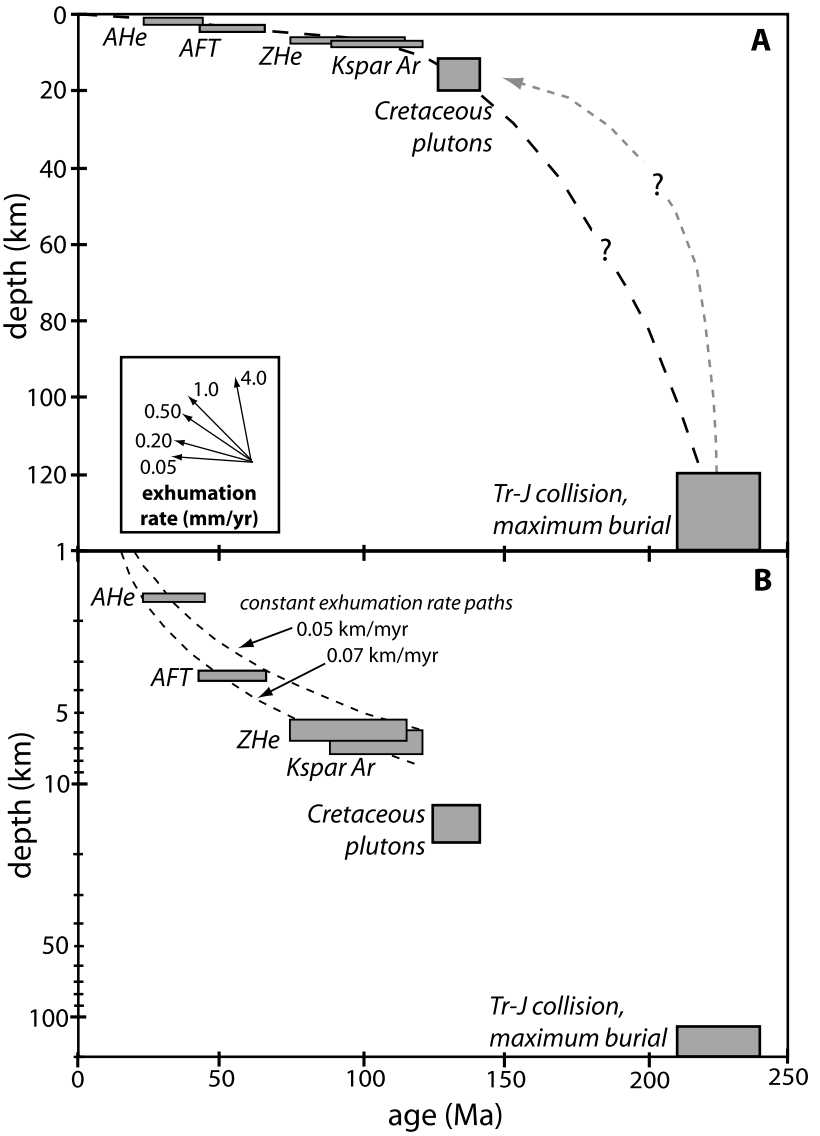

Fig. 9. Crustal depth as a function of age, for rocks in the core of the Dabie Shan. Triassic metamorphism is estimated as 120-140 km at 215-240 Ma (for example, Liou and others, 1996; Hacker and others, 1996; 2000). "Cretaceous plutons" box outlines approximate emplacement depths (from Al-in-hornblende; Ratschbacher and others, 2000) and crystallization ages (Hacker and others, 1998) of Cretaceous magmatic bodies in the core of the range. "Kspar Ar" is 90-120 Ma "reheating" event of Ratschbacher and others (2000), interpreted as cooling through ~200°C at this time. (U-Th)/He and fission-track closure depths are taken from steady exhumation models discussed in text, assuming pre-exhumational geothermal gradients of 25°C; ages represent the ranges for each system observed in the core of the Dabie Shan (see figure 1). Inset in A: instantaneous exhumation rate. Dashed lines are possible depth-age trajectories of range-core rocks. In B, depths corresponding to the 200°C and 180°C inferred closure temperatures of the K-feldspar $^{40}Ar/^{39}Ar$ ("Kspar Ar") and zircon He ("ZHe") are shown for a possible range of 25°-30 °C, due to possible higher gradients following the Cretaceous orogenic event. Dashed lines in part B represent depth-time paths of constant exhumation rates of 0.05 and 0.07 km/myr since 120 Ma. These rates bracket the 0.06 ± 0.01 km/myr exhumation rate for the range-core implied by best-fit model cooling paths shown in figure 8, as well as model exhumation rates for individual samples in the range-core shown in figure 2.

8 kilometers of exhumation has occurred in the core of the Dabie Shan in the last 100 myr. Figure 9B also reinforces the interpretation that a constant exhumation rate of 0.06 ± 0.01 km/myr can explain the apparent depth-time relationships of data with closure temperatures lower than about 200°C, or since ~100 Ma.

CONCLUSION

Apatite and zircon (U-Th)/He ages from the Dabie Shan show cross-range age distributions consistent with a gradient in erosional exhumation rates between the range-flanks and range-core over the last ~100 Ma. Apatite He ages indicate average exhumation rates since the middle Tertiary were as low as 0.02 km/myr on the range flanks, to as high as 0.06 km/myr in the range core. We also used an admittance ratio model to correct the age-elevation relationship of apatite He ages in a vertical transect in the core of the range and derive model exhumation rates. These results indicate an exhumation rate as low as 0.05 km/myr and as high as 0.07 km/myr in the range core since the mid-Tertiary. Thermal modeling of the apatite He and zircon He ages and apatite fission-track ages in the range-core vertical transect also suggest a long-term exhumation rate of 0.06 ± 0.01 km/myr, that may have been constant since as early as the mid-Cretaceous. Some details of the ZHe and AFT data suggest modestly increased exhumation rates in the Late Cretaceous through early Tertiary, but none of these data support an increase in exhumation rates later than about 60 Ma. Most of the ages in the Dabie Shan represent steady-rate exhumation ages, not exhumation rate changes due to discrete tectonic or erosional events. Finally, this study represents the first large-scale application of zircon (U-Th)/He thermochronometry to regional exhumation problems, and supports the efficacy of the technique for providing constraints on timing and rates of crustal exhumation through depths corresponding to temperatures greater than those of apatite fission-track, but less than those of K-feldspar Ar dating.

ACKNOWLEDGMENTS

We thank Ethan Baxter, Brad Hacker, Danny Stockli, and Kelin Whipple for constructive reviews, Jim Spotila for helpful comments, and Jean Braun and Lothar Ratschbacher for enlightening discussions about topographic effects and regional geology, respectively. Acknowledgment is made to the U.S. NSF for grant EAR-9909996, to NFS-China for grant 40272093, to MOST-China for grant G2000078501, and to the Donors of The Petroleum Research Fund, administered by the American Chemical Society, for partial support of this research.

APPENDIX A

ANALYTICAL PROCEDURES

(U-Th)/He Chronometry

Apatite and zircon (U-Th)/He ages were performed at Yale and Washington State Universities by both furnace and laser (both CO_2 and Nd-YAG) heating for He extraction, and both quadrupole and sector ICP-MS for U-Th determinations. All samples in the vertical transect (samples DB40-45 in table 1) were dated by single-grain, Nd-YAG laser heating and sector ICP-MS methods at Yale; procedures for other samples were similar.

Dated crystals were hand-picked from separates (see fission-track procedures) with high power (160x) stereo-zoom microscopes with cross-polarization for screening inclusions. Selected crystals were measured and digitally photographed in at least 2 different orientations, for alpha-ejection corrections. Crystals were loaded into 1-mm Pt foil tubes (in some cases, Mo was used for zircon), which were then loaded into copper or stainless steel sample planchets with 30 sample slots. Planchets were loaded into a ~10 centimeter laser cell with sapphire (or ZnS for the CO_2 laser) window, connected by high-vacuum flexhose to the He extraction/measurement line. Once in the laser cell and pumped to 10^{-7}-10^{-8} torr, crystal-bearing foil tubes were individually heated by lasing with about 1-5 W on the Nd-YAG, or 5-15 W on the CO_2, laser, for three minutes for apatite or 20 minutes for zircon. Temperatures of heated foil packets were not measured, but

from experiments relating luminosity and step-wise degassing of both apatite and zircon, we estimate typical heating temperatures of 1000° to 1200°C for apatite, and 1250° to 1400°C for zircon. ^{4}He blanks (0.05-0.5 femtomol ^{4}He, after correction for ^{4}He in the spike) were determined by heating empty foil packets using the same procedure. Crystals were checked for quantitative degassing of He by sequential reheating. While apatites rarely exhibited residual gas after the first degassing, about 50 percent of zircons did, and frequently required 2 to 3 reheatings to reduce the yield to <1 to 2 percent of the original extract. Gas liberated from samples was processed by: 1) spiking with ~0.4 pmol of ^{3}He, 2) cyrogenic concentration at 16K on a charcoal trap (condensation time calibrated for no significant ^{4}He/^{3}He fractionation), and purification by release at 37K, and 3) measurement of ^{4}He/^{3}He ratios (corrected for HD and H_3 by monitoring H^+) on a quadrupole mass spectrometer next to a cold Zr-alloy getter. All ratios were referenced to multiple same-day measured ratios and known volumes of ^{4}He standards processed in the same way. Linearity of this standard referencing procedure has been confirmed over four orders of magnitude of ^{4}He intensity. ^{4}He standard reproducibility averages 0.2 percent on a daily and long-term (tank-depletion corrected) basis. Estimated 2σ analytical uncertainty on sample He determinations, including precision and accuracy from original manometric ^{4}He standard calibrations, is 1 to 2 percent.

Following degassing, samples were retrieved from the laser cell, spiked with a calibrated ^{229}Th and ^{233}U solution, and dissolved. Apatites were dissolved *in-situ* from Pt tubes in ~30 percent HNO_3 in teflon vials. Zircons were removed from foil and then dissolved in teflon microvials in Parr bombs with HF and HNO_3, followed by HCl and/or H_3BO_3 to remove fluoride salts, and a final dissolution in HNO_3. Each sample batch was prepared with a series of acid blanks and spiked normals to check the purity and calibration of the reagents and spikes. Spiked solutions were analyzed as 0.5 ml of ~1-5 ppb U-Th solutions by isotope dilution on a Finnigan Element2 ICP-MS with a teflon micro-flow nebulizer and double-pass spray chamber. Procedural U and Th blanks by this method are 1 ± 0.5 pg and 2 ± 1 pg, respectively. Routine in-run precisions and long-term reproducibilities of standard ^{232}Th/^{229}Th and ^{238}U/^{233}U are 0.1 to 0.4 percent, and estimated uncertainty on sample U-Th contents are estimated to be 1 to 2 percent (2σ).

Alpha ejection was corrected using the method of Farley and others (1996), modified by Farley (2002). Replicate analyses of Durango apatite and Fish Canyon Tuff zircon during the period of these analyses yielded mean ages of 32.5 ± 1.5 Ma (2σ; n=41) and 28.3 ± 2.4 Ma (2σ; n=37), respectively. On the basis of reproducibility of these and other intralab standards, we estimate an analytical uncertainty of 6 percent and 8 percent (2σ) for apatite and zircon age determinations, respectively, in this study.

Apatite Fission-Track Chronometry

Apatite grains were mounted in epoxide resin cured at 90°C for 1 hour, and all grain mounts were polished using 3.0 μm Al_2O_3 and then 0.3 μm Al_2O_3 slurries on a polishing wheel to expose internal crystal surfaces. Grains were etched in 5.5N HNO_3 for 20.0 (±0.5) seconds at 21 (±1) °C to reveal spontaneous fission tracks. After spontaneous fission-track densities were measured for the apatite grains of interest, grains were irradiated with ^{252}Cf-derived fission fragments (Donelick and Miller, 1991) in a nominal vacuum and then re-etched in 5.5N HNO_3 for 20.0 (±0.5) seconds at 21 (±1) °C to reveal the ^{252}Cf-derived fission tracks and any spontaneous confined fission tracks. Length measurements were performed only on horizontal, confined, spontaneous fission tracks with well-defined ends lying in planes parallel to the crystallographic c-axis (all ^{252}Cf-derived fission tracks are incident upon the etched apatite surface and are therefore not confined within the grain). Measurements were performed using an optical microscope and a combination of reflected and unpolarized transmitted light at a magnification of 1562.5x (100x dry objective, 1.25x projection tube, and 12.5x oculars). Full details on the methods used are summarized in Donelick (1991).

Apatite grains were classified according to their kinetics of fission-track annealing (the rate at which fission tracks are lost), inferred using parameter Dpar (units μm). Dpar is the fission-track etch pit diameter parallel to the crystallographic c-axis at the polished, etched, and analyzed apatite surface (Crowley and others, 1991; Naeser, 1992; Donelick, 1993; Burtner and others, 1994; Grønlie and others, 1994; Donelick, 1995). Dpar exhibits general but imperfect correlations with apatite fission-track annealing kinetics (Carlson and others, 1999; Ketcham and others, 1999), and chemical composition (Burtner and others, 1994), with small Dpar (2.00 μm) grains typical of fast-annealing, Ca-F-apatite and large Dpar grains typical of slow- to fast-annealing Ca(±Fe, Mn, rare earth elements)-F(±Cl)(±OH)-apatite. Dpar is at least as reliable as Cl- or OH-content for constraining apatite fission-track annealing kinetics (Carlson and others, 1999; Donelick, unpublished data). The parameter Dpar, calculated as the arithmetic mean of between 1 and 4 individual Dpar values per grain, was determined for each apatite grain that yielded either fission-track age data or track length data. Full details of the methods used are summarized in Burtner and others (1994).

Fission-track ages were determined using the external detector method and all counting was performed using an optical microscope (details as in first paragraph of this section). Polished and etched grain mounts were covered by thin sheets of low-uranium muscovite mica prior to neutron irradiation; for purposes of standardization, similar sheets of muscovite were placed in direct contact with small chips of CN-1 U-doped glass (courtesy of Dr. Jan Schreurs, Corning Glass Works, Corning, New York). The samples (together with their respective CN-1 glass standards) were irradiated for 45 minutes (nominal thermal-neutron fluence of about 10^{16} neutrons/cm^2) in position D-9 in the nuclear reactor at Washington State University (1 MW power level). After irradiation, the short-lived radionuclides in the samples were allowed to decay to background levels before further analyses were performed. Once removed from the samples and glass standards, mica sheets were etched for 12 minutes in 48 percent HF at 24°C, revealing the induced (formed by irradiation in the reactor) fission tracks for optical viewing. Fission track ages were calculated using a zeta calibration factor of 113.8 ± 2.9 for Fish Canyon Tuff and Durango apatite age standards (Hurford and Green, 1983).

References

Baldwin, J. A., Whipple, K. X., and Tucker, G. E., 2003, Implications of the shear stress river incision model for the timescale of postorogenic decay of topography: Journal of Geophysical Research, v. 108, doi: 10.1029/2001JB000550.

Brandon, M. T., Roden-Tice, M. K., and Garver, J. I., 1998, Late Cenozoic exhumation of the Cascadia accretionary wedge in the Olympic Mountains, northwest Washington State: Geological Society of America Bulletin, v. 110, p. 985–1009.

Braun, J., 2002a, Quantifying the effect of recent relief changes on age-elevation relationships: Earth and Planetary Science Letters, v. 200, p. 331–343.

——— 2002b, Estimating exhumation rate and relief evolution by spectral analysis of age-elevation datasets: Terra Nova, v. 14, p. 210–214.

Burtner, R. L., Nigrini, A., and Donelick, R. A., 1994, Thermochronology of Lower Cretaceous source rocks in the Idaho-Wyoming thrust belt: American Association of Petroleum Geologists Bulletin, v. 78, n. 10, p. 1613–1636.

Carlson, W. D., Donelick, R. A., and Ketcham, R. A., 1999, Variability of apatite fission track annealing kinetics I: Experimental results: American Mineralogist, v. 84, p. 1213–1223.

Crowley, K. D., Cameron, M., and Schaefer, R. L., 1991, Experimental studies of annealing of etched fission tracks in fluorapatite: Geochimica et Cosmochimica Acta, v. 55, p. 1449–1465.

Donelick, R. A., 1991, Crystallographic orientation dependence of mean etchable fission track length in apatite: An empirical model and experimental observations: American Mineralogist, v. 76, p. 83–91.

——— 1993, A method of fission track analysis utilizing bulk chemical etching of apatite: U.S. Patent Number 5,267,274.

——— 1995, A method of fission track analysis utilizing bulk chemical etching of apatite: Australian Patent Number 658,800.

Donelick, R. A., and Miller, D. S., 1991, Enhanced TINT fission track densities in low spontaneous track density apatites using ^{252}Cf-derived fission fragment tracks: A model and experimental observations: Nuclear Tracks and Radiation Measurements, v. 18, p. 301–307.

Ducea, M. N., and Saleeby, J .B., 1998, A case for delamination of the deep batholithic crust beneath the Sierra Nevada, California: International Geology Review, v. 40, p. 78–93.

Ehlers, T. A., and Farley, K. A., 2003, Apatite (U-Th)/He thermochronology: methods and applications to problems in tectonics and surface processes: Earth and Planetary Science Letters, v. 206, p. 1–14.

Ehlers, T. A., Armstrong, P. A., and Chapman, D. S., 2001, Normal fault regimes and the interpretation of low-temperature thermochronometers: Physics of the Earth and Planetary Interiors, v. 126, p. 179–194.

Eide, E. A., McWilliams, M. O., and Liou, J. G., 1994, ^{40}Ar/^{39}Ar geochronology and exhumation of high-pressure to ultrahigh-pressure metamorphic rocks in east-central China: Geology, v. 22, p. 601–604.

Farley, K. A., 2000, Helium diffusion from apatite: General behavior as illustrated by Durango fluorapatite: Journal of Geophysical Research, v. 105, p. 2903–2914.

——— 2002, (U-Th)/He dating: Techniques, calibrations, and applications: Mineralogical Society of America, Reviews in Mineralogy and Geochemistry, v. 47, p. 819–844.

Farley, K. A., Wolf, R. A., and Silver, L. T., 1996, The effects of long alpha-stopping distances on (U-Th)/He ages: Geochimica et Cosmochimica Acta, v. 60, p. 4223–4229.

Fitzgerald, P. G., Sorkhabi, R. B., Redfield, T. F., and Stump, E., 1995, Uplift and denudation of the central Alaska Range: A case study in the use of apatite fission-track thermochronology to determine absolute uplift parameters: Journal of Geophysical Research, v. 100, 20,175–20,191.

Gallagher, K., Brown, R. W., and Johnson, C. J., 1998, Geological applications of fission track analysis: Annual Reviews of Earth and Planetary Sciences, v. 26, p. 519–572.

Grimmer, J. C., Jonckheere, R., Enkelmann, E., Ratschbacher, L., Hacker, B. R., Blythe, A. E., Wagner, G. A., Wu, Q., Liu, S., and Dong, S., 2002, Cretaceous-Cenozoic history of the southern Tan-Lu fault zone: apatite fission-track and structural constraints from the Dabie Shan (eastern China): Tectonophysics, v. 359, p. 225–253.

Grimmer, J. C., Ratschbacher, L., McWilliams, M., Franz, L., Gaitzch, I., Tichomirowa, M., Hacker, B. R., and Zhang, Y., 2003, When did the ultra-high pressure rocks reach the surface? A $^{207}Pb/^{206}Pb$ zircon, $^{40}AR/^{39}AR$ white mica, Si-in-white mica, single-grain provenance study of Dabie Shan synorogenic foreland sediments: Chemical Geology, v. 197, p. 87–110.

Grønlie, A., Naeser, C. W., Naeser, N. D., Mitchell, J. G., Sturt, B. A., and Ineson, P. R., 1994, Fission-track and K-Ar dating of tectonic activity in a transect across the Møre-Trøndelag Fault Zone, central Norway: Norsk Geologisk Tidsskrift, v. 74, p. 24–34.

Hacker, B. R., and Wang, Q. C., 1995, Ar/Ar geochronology of ultrahigh-pressure metamorphism in central China: Tectonics, v. 14, p. 994–1006.

Hacker, B. R., Wang, X., Eide, E. A., and Ratschbacher, L., 1996, The Qinling-Dabie ultra-high-pressure collisional orogen, *in* Yin, A., and Harrison, T. M., editors, The tectonic evolution of Asia: Cambridge, Cambridge University Press, p. 345–370.

Hacker, B. R., Ratschbacher, L., Webb, L., Ireland, T., Walker, D., and Dong, S., 1998, U/Pb zircon ages constrain the architecture of the ultrahigh-pressure Qinling-Dabie Orogen, China: Earth and Planetary Science Letters, v. 161, p. 215–230.

Hacker, B. R., Ratschbacher, L., Webb, L., McWilliams, M. O., Ireland, T., Calvert, A., Dong, S., Wenk, H. R., and Chateigner, D., 2000, Exhumation of ultrahigh-pressure continental crust in east central China: Late Triassic-Early Jurassic tectonic unroofing: Journal of Geophysical Research, v. 105, p. 13,339–13,364.

House, M. A., Wernicke, B. P., and Farley, K. A., 1998, Dating topography of the Sierra Nevada, California, using apatite (U-Th)/He ages: Nature, v. 396, p. 66–69.

——— 2001, Paleo-geomorphology of the Sierra Nevada, California, from (U-Th)/He ages in apatite: American Journal of Science, v. 301, p. 77–102.

Hu, S., He, L., and Wang, J., 2000, Heat flow in the continental area of China: a new data set: Earth and Planetary Science Letters, v. 179, p. 407–419.

Hurford, A. J., and Green, P. F., 1983, The zeta age calibration of fission-track dating: Chemical Geology, v. 1, p. 285–317.

Jull, M., and Kelemen, P. B., 2001, On the conditions for lower crustal convective instability: Journal of Geophysical Research, v. 106, p. 6423–6446.

Kern, H., Gao, S., Jin, Z., Popp, T., and Jin, S., 1999, Petrophysical studies on rocks from the Dabie ultrahigh-pressure (UHP) metamorphic belt, Central China: implications for the composition and delamination of the lower crust: Tectonophysics, v. 301, p. 191–215.

Ketcham, R. A., Donelick, R. A., and Carlson, W. D., 1999, Variability of apatite fission track annealing kinetics III: Extrapolation to geological time scales: American Mineralogist, v. 84, p. 1235–1255.

Ketcham, R. A., Donelick, R. A., and Donelick, M. B., 2000, AFTSolve: A program for multi-kinetic modeling of apatite fission-track data: Geological Materials Research, v. 2, n. 1.

Kirby, E., Reiners, P. W., Krol, M., Hodges, K., Farley, K. A., Whipple, K., Yiping, L., Tang, W., and Chen, Z., 2002, Late Cenozoic uplift and landscape evolution along the eastern margin of the Tibetan plateau: Inferences from $^{40}Ar/^{39}Ar$ and U-Th-He thermochronology: Tectonics, 10.1029/2000TC001246.

Liou, J. G., Zhang, R. Y., Wang, X., Eide, E. A., Ernst, W. G., and Maruyama, S., 1996, Metamorphism and tectonics of high-pressure and ultra-high pressure belts in the Dabie-Sulu region, China, *in* Yin, A., and Harrison, T. M., editors, The tectonic evolution of Asia: Cambridge, Cambridge University Press, p. 300–344.

Mancktelow, N. S., and Grasemann, B., 1997, Time-dependent effects of heat advection and topography on cooling histories during erosion: Tectonophysics, v. 270, p. 167–195.

Molnar, P., and Tapponnier, P., 1975, Cenozoic tectonics of Asia: Effects of a continental collision: Science, v. 189, p. 419–426.

Naeser, N. D., 1992, Miocene cooling in the southwestern Powder River Basin, Wyoming - Preliminary evidence from apatite fission-track analysis: U.S. Geological Survey Bulletin 1917-O, 17 p.

Nie, S., Yin, A., Rowley, D. B., and Jin, Y., 1994, Exhumation of the Dabie Shan ultra-high-pressure rocks and accumulation of the Songpan-Ganzi flysch sequence, central China: Geology, v. 22, p. 999–1002.

Northrup, C. J., Royden, L. H., and Burchfiel, B. C., 1995, Motion of the Pacific plate relative to Eurasia and its potential relation to Cenozoic extension along the eastern margin of Eurasia: Geology, v. 23, p. 719–722.

Okay, A. I., Sengor, A. M. C., and Satir, M., 1993, Tectonics of an ultrahigh-pressure metamorphic terrane: The Dabie Shan/Tongbai Shan orogen, China: Tectonics, v. 12, p. 1320–1334.

Pazzaglia, F. J., and Brandon, M. T., 1996, Macrogeomorphic evolution of the post-Triassic Appalachian Mountains determined by deconvolution of the offshore basin sedimentary record: Basin Research, v. 8, p. 255–278.

Peltzer, G., Tapponnier, P., Zhang, Z. T., and Xu, Z. Q., 1985, Neogene and Quaternary faulting along the Qinling Shan: Nature, v. 317, p. 500–505.

Ratschbacher, L., Hacker, B. R., Webb, L. E., McWilliams, M., Ireland, T., Dong, S., Calvert, A., Chateigner, D., and Wenk, H. R., 2000, Exhumation of the ultrahigh-pressure continental crust in east central China: Cretaceous and Cenozoic unroofing and the Tan-Lu fault: Journal of Geophysical Research, v. 105, p. 13,303–13,338.

Reiners, P. W., and Spell, T. L., 2002, Intercalibration of zircon (U-Th)/He and K-feldspar $^{40}Ar/^{39}Ar$ thermochronometry: Geochimica et Cosmochimica Acta, v. 66, p. A631.

Reiners, P. W., Farley, K. A., and Hickes, H. J., 2002, He diffusion and (U-Th)/He thermochronometry of zircon: Initial results from Fish Canyon Tuff and Gold Butte: Tectonophysics, v. 349, p. 247–308.

Rowley, D. B., Xue, F., Tucker, R. D., Peng, Z. X., Baker, J., and Davis, A., 1997, Ages of ultrahigh pressure metamorphism and protolith orthogneisses from the eastern Dabie Shan: U/Pb zircon geochronology: Earth and Planetary Science Letters, v. 151, p. 191–203.

Schmid, R., Ryberg, T., Ratschbacher, L., Schulze, A., Franz, L., Oberhänsli, R., and Dong, S., 2001, Crustal structure of the eastern Dabie Shan interpreted from deep reflection and shallow tomographic data: Tectonophysics, v. 333, p. 347–359.

Stüwe, K., and Hintermüller, M., 2000, Topography and isotherms revisited: The influence of laterally migrating drainage divides: Earth and Planetary Science Letters, v. 184, p. 287–303.

Stüwe, K., White, L., and Brown, R., 1994, The influence of eroding topography on steady-state isotherms. Application to fission track analysis: Earth and Planetary Science Letters, v. 124, p. 63–74.

Tapponnier, P., and Molnar, P., 1977, Active faulting and tectonics in China: Journal of Geophysical Research, v. 82, p. 2905–2930.

Tapponnier, P., Peltzer, G., and Armijo, R., 1986, On the mechanics of the collision between India and Asia, *in* Coward, M. P., and Ries, A. C., editors, Collision tectonics: Geological Society Special Publication No. 19, p. 115–157.

Turcotte, D. L., and Schubert, G., 1982, Geodynamics: New York, John Wiley and Sons, 450 p.

——— 2002, Geodynamics, 2nd Edition: New York, Cambridge University Press, 456 p.

Wang, Q., Zhang, P. Z., Freymueller, J. T., Bilham, R., Larson, K. M., Lai, X., You, X., Niu, Z., Wu, J., Li, Y., Liu, J., Yang, Z., and Chen, Q., 2001, Present-day crustal deformation in China constrained by global positioning system measurements: Science, v. 294, p. 574–577.

Webb, L. E., Hacker, B. R., Ratschbacher, L., McWilliams, M. O., and Dong, S., 1999, Thermochronologic constraints on deformation and cooling history of high- and ultrahigh-pressure rocks in the Qinling-Dabie orogen, eastern China: Tectonics, v. 18, p. 621–638.

Wolf, R. A., Farley, K. A., and Silver, L. T., 1996, Helium diffusion and low-temperature thermochronometry of apatite: Geochimica et Cosmochimica Acta, v. 60, p. 4231–4240.

Wolf, R. A., Farley, K. A., and Kass, D. M., 1998, Modeling of the temperature sensitivity of the apatite (U-Th)/He thermochronometer: Chemical Geology, v. 148, p. 105–114.

Xue, A., and Jin, W., 2001, Petroleum geology of Hefei Basin and the tectonic coupling between Hefei Basin and Dabie Orogen: China, Petroleum Industry Press, 173 p.

Xue, F., Rowley, D. B., and Baker, J., 1996, Refolded syn-ultrahigh-pressure thrust sheets in the south Dabie complex, China: Field evidence and tectonic implications: Geology, v. 24, p. 455–458.

Xue, F., Rowley, D. B., Tucker, R. D., and Peng, Z. X., 1997, U-Pb zircon ages of granitoid rocks in the North Dabie Complex, Eastern Dabie Shan, China: Journal of Geology, v. 105, p. 744–753.

Xue-Cheng, Y., Klemperer, S. L., Wen-Bang, T., Lai-Xiang, L., and Chetwin, E., 2003, Crustal structure and exhumation of the Dabie Shan ultrahigh-pressure orogen, eastern China, from seismic reflection profiling: Geology, v. 31, p. 435–438.

Yin, A., and Nie, S., 1993, An indentation model for the North and South China collision and the development of the Tan-Lu and Honam fault systems, Eastern Asia: Tectonics, v. 12, p. 801–813.

Zhang, R. Y., Shu, J. F., Mao, H. K., and Liou, J. G., 1999, Magnetite lamellae in olivine and clinohumite from Dabie UHP ultramafic rocks, central China: American Mineralogist, v. 84, p. 564–659.